Nanoindentation of Inherently Conductive Polyaniline Films

A DESIGN PROJECT
SUBMITTED TO THE FACULTY OF THE GRADUATE SCHOOL
OF THE UNIVERSITY OF MINNESOTA
BY

Jeremy Kenneth Dworshak

IN PARTIAL FULFILLMENT OF THE REQUIREMENTS
FOR THE DEGREE OF
Master of Material Science and Engineering

William W. Gerberich

February, 2011

Acknowledgements

There are many people that have earned my gratitude for their contribution to my time in graduate school.

To all listed here and others unintentionally omitted thank you,...

Stacey, for the support and encouragement to dedicate time for completion of this thesis.

Professor Bill Gerberich, for the academic advisement on compiling and evaluating the data.

Douglas Stauffer, for the training and experimental guidance when performing the nanoindentation trials.

Maureen Steinwall, for creating and sustaining a "learning organization."

Hysitron, for the equipment usage and time at their facility to conduct the research.

Savannah and Jaron, for the motivation to finish so I can spend more time with you!

Dedication

This thesis is a culmination of my academic efforts. My life long journey of learning will continue past this point, yet the memories of this milestone will not be forgotten.

Thank you to all who have loved and supported me along the way.

Abstract

Conducting polymers (CPs) are similar to semiconductors in the fact that they can be used in electrical, optical, and magnetic devices. The microstructure enabling CPs to be used in these devices is the presence of π-electron conjugation or, more simply, the presence of double bonds in the polymer structure.

This structure differentiates CPs from semiconductors. CPs, made from organic π-electron materials, are typically amorphous polymeric materials. This is unlike semiconductors, which are prominently atomic solids. This structure difference allows for nearly limitless conducting mechanisms to be present in CPs. Additionally, the amorphous structure allows for varying physical and mechanical properties to fit in a variety of new applications.

The study of CPs is very dynamic and has evolved from early light weight battery applications. The evolution of CPs has brought forth its use in electroluminescence, photorefractivity, electrochromism, optical nonlinearity, and sensing devices. These new and former applications are continually being applied to devices on a smaller and smaller size scale. Thus, magnifying the need to understand nano-scale properties.

This thesis examines the nanoindentation and conductive properties of CPs. Nanoindentation of four polyaniline (PANI) films cast on glass slides are evaluated. The effect of carbon nanotube filler is evaluated with regard to its effect on indentation depth and conductivity of the overall film.

The results show a trend of increasing conductance with higher application of pressure. This may be the result of a morphology change of the film. The addition of carbon nanotubes result in a decrease in conductivity. This non-intuitive result is likely due to porosity or voids at the carbon nanotube-polymer interface.

Contents

List of Tables

List of Figures

Chapter 1

Polymers

1.1 Traditional Polymers

Polymers are defined as molecules made up of smaller molecules that are joined together by chemical bonds [1]. These molecules are chemical elements that when combined form specific polymers with distinct and measurable properties.

The elements that polymers are comprised of are typically hydrogen, carbon, oxygen, and nitrogen. These elements have differing chemical properties which affect the type of reactions the molecule participates in. Thus, the specific elements can be combined with other elements to form unique molecules. These molecules are then joined together, in various ways, to form a chain of molecules.

Polymers are covalently bonded materials primarily comprised of carbon and hydrogen. Covalent bonds are defined as the "sharing" of electrons [2]. The type of covalent bond dictates the electrical properties of the polymer.

Common polymers consist of single or σ-bonds between the elements. From a quantum mechanics perspective, the electrons are shared in the s-orbital. There is considerable of overlap between the s-orbitals, which gives the σ-bond a high degree of bond strength.

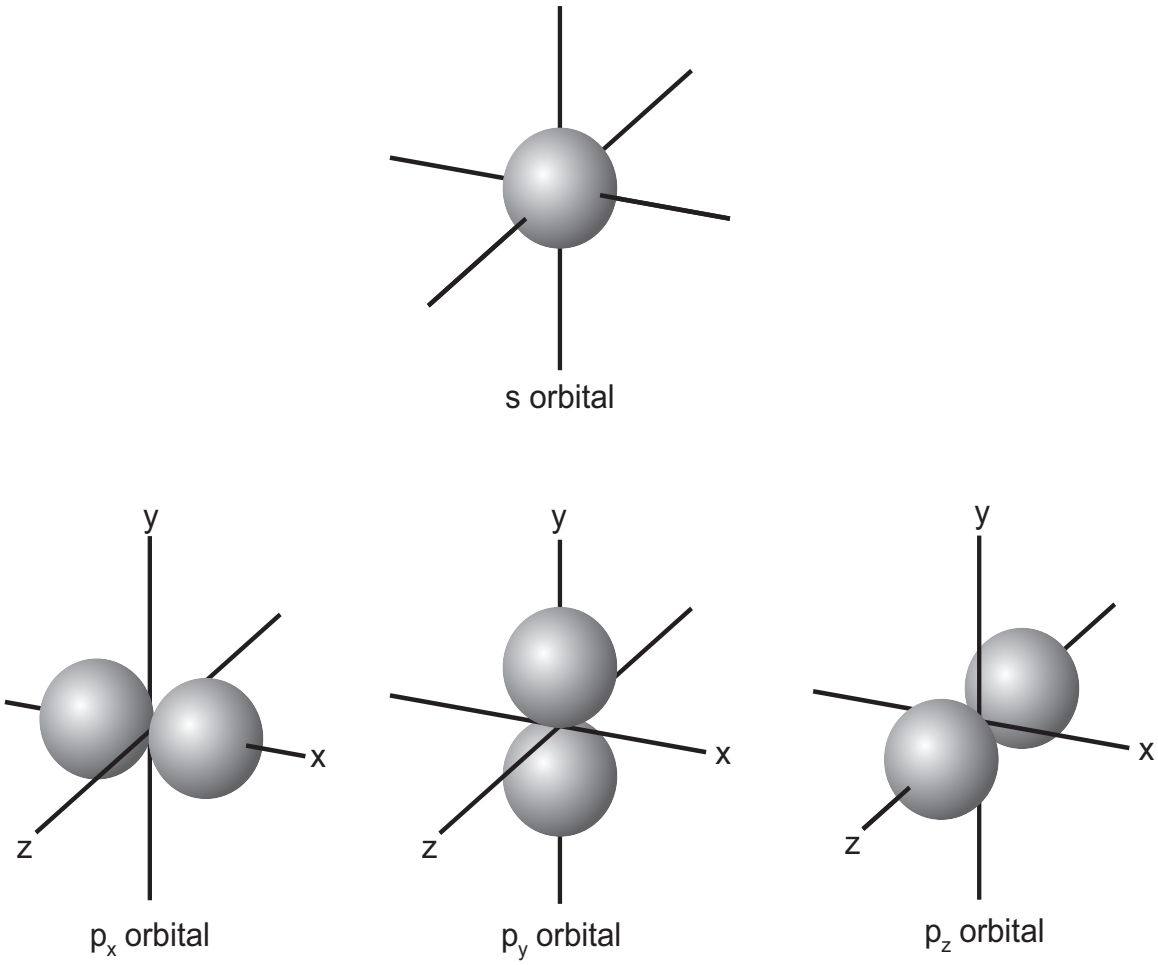

Figure 1.1: Electron Cloud Orbitals

This image shows the spatial differences between s- and p-orbitals. The shaded regions represent the locations of the electron(s).

This overlap of the two electrons, shared between the two elements, creates a saturated bond. This type of bonding does not allow for conductivity to occur. Materials containing only these types of bonds are classified as insulators; e.g. polypropylene.

These molecules are either synthetically made or can be naturally occurring. It is the naturally occurring variety that started it all. There are some early biblical references

(Exodus and Genesis) to "slime," which is thought to have been a form of bitumen. Bitumen is a naturally occurring polymer and may have been the first one used in human history: It still has use today in asphalt.

Other naturally occurring resins were also used in history. Shellac, for instance, has seen use for over 3000 years as a coating on materials to protect them and make them appear glossy. Later in history, patents were submitted for uses of shellac as early as 1868 [3].

These naturally occurring polymers have mechanical limitations. It is the limitations of these polymers that propelled individuals into attempting to modify them. The earliest documented successes of modifying natural polymers involved coagulated rubber. It was found through modifying the rubber with molten sulphur the material retained its elastic properties over a wider range of temperatures. This realization resulted in patents being placed by Thomas Hancock and Charles Goodyear [3].

This modification of naturally occurring polymers is significant! It is a precursor to the current research area of polymer synthesis. It opened the potential for polymers to be completely synthetic. Which, in fact, is what started then to occur.

A common "first" polymer taught to students is celluloid. This material was initially researched by Pelouze, Schonbein and others. Alexander Parkes, however, researched it further and attempted to commercialize the manufacture and sale of this resin. His company, Parkesine Company, failed - however, it is an important note that Parkes was the first man to attempt commercialization of a chemically modified polymer [3].

John Wesley Hyatt then entered the scene and developed a method for manufacturing billiard balls out of celluloid in the 1860's. The success of this industry spurred future work in the development of other polymers [3].

This takes us to the early 1900's. At this time, only a few polymers were available for use; shellac, gutta, percha, ebonite, and celluloid. It's amazing to think that there are now over 30,000 thermoplastic materials now available only 100 years later!

The early 1900's saw investigative work in the area of phenolics. The first commercialized version was brought about by Leo Hendrik Baekeland with the formation of the General Bakelite Company. This success stimulated further polymer synthesis work, namely urea-formaldehyde reactions. This precursor to polyurethane resins allowed plastics to be made into light colored articles, unlike phenolics.

Further exploratory research leads us to the common engineering resins used today; polyamides (nylon), polytetrafluoroethylene (teflon), polyethylene, polypropylene, polyvinylchloride, and many others.

These above mentioned polymers are all deemed non-conducting, or more appropriately as insulating. This characteristic is a common conclusion in most polymers due to the polymerization technique employed to synthesize them.

Traditional polymers are synthesized in two primary ways; addition polymerization and step-growth polymerization. Each of these methods result in a saturated polymer chain; single carbon-carbon bonds dominate the structure. These single bonds are called sigma bonds.

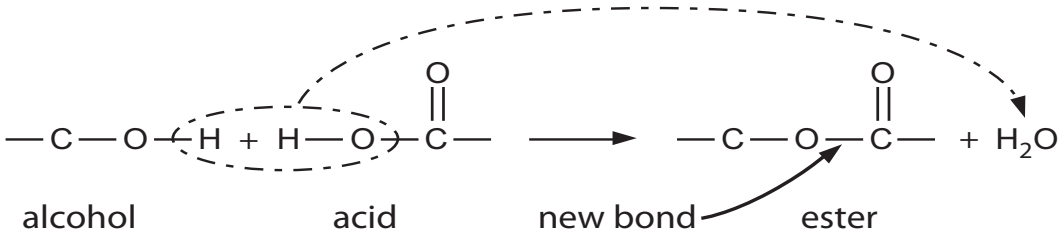

(a) Reaction of an alcohol and an acid to make an ester and water

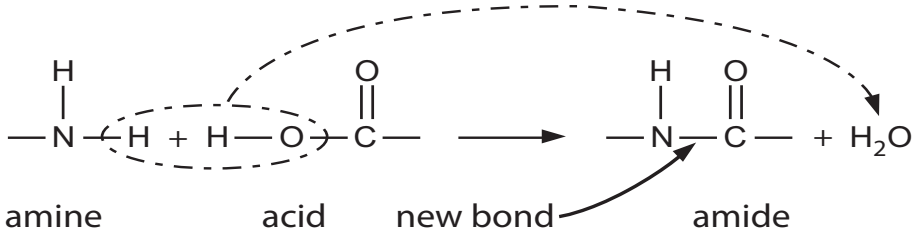

(b) Reaction of an amine and an acid to make an amide and water

Figure 1.2: Step Growth Polymerization [1]

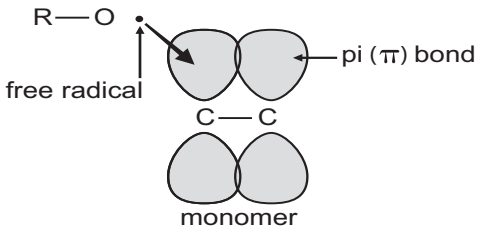

(a) Peroxide free radical interaction with monomer π-bond

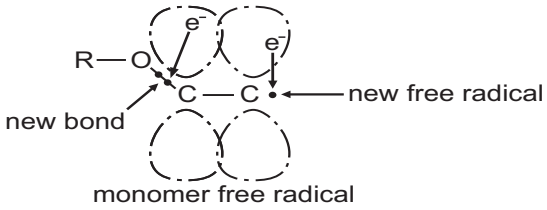

(b) Peroxide-carbon bond formed and transfer of free radical to distant carbon

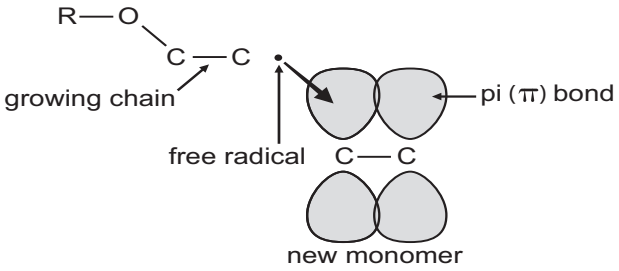

(c) Carbon free radical interaction with π-bond in new monomer

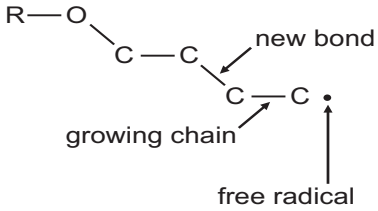

(d) Chain lengthening (propagation) step

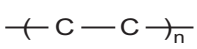

(e) Polymer representation (repeating unit only)

Figure 1.3: Chain Growth Polymerization [1]

Certain polymers polymerized in this way were noted to have an amount of double bonds present; e.g. *pi*-bonds. Polyacetylene, polymerized in 1971, was found to have some conductivity along its chain length [4]

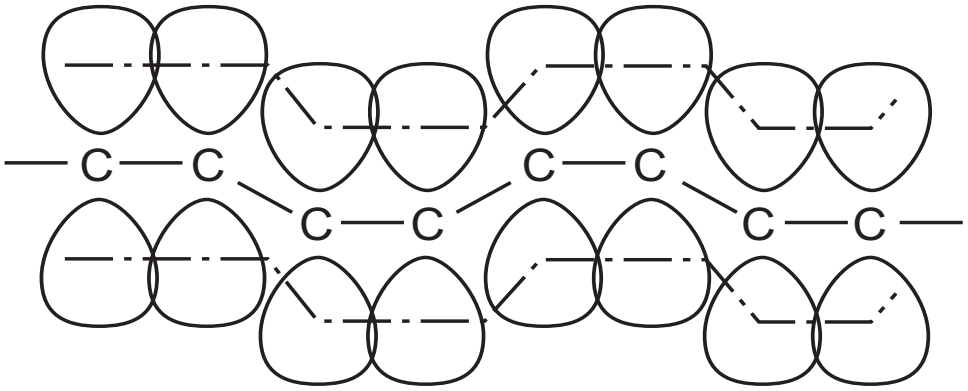

Figure 1.4: p-orbital Overlap

Chemical structure of polyacetylene detailing the overlap of p-orbitals. This overlap leads to the ability of the polymer to conduct electricity[1].

Polyacetylene can be made conductive across other directions by incorporating molecules with free electrons. This allows conductivity in directions other than just along the polymer chain.

It is this exploration into improving the conductivity of polymers that brings us into our next section; conducting polymers.

1.2 Conducting Polymers (CPs)

When considering the electrical properties of plastics, one might initially think of a common plastic (e.g. polyethylene) which is insulating and does not conduct very well. This inherent property of "common" plastics is due to the dominant characteristic of σ-bonds (see discussion above). Polymers can be conductive, however, through a variety of different ways. Yet, prior to discussing how polymers are conductive. Let's

first discuss what is meant for a material to be classified as conductive.

Materials are separated into three broad categories with respect to their conductivity properties; metals, insulators, and semiconductors. An individual material has a valence band and a conduction band, based on its electron configuration. Space exists between the two bands. That space is termed the band gap. Pictorially, here are the three categories:

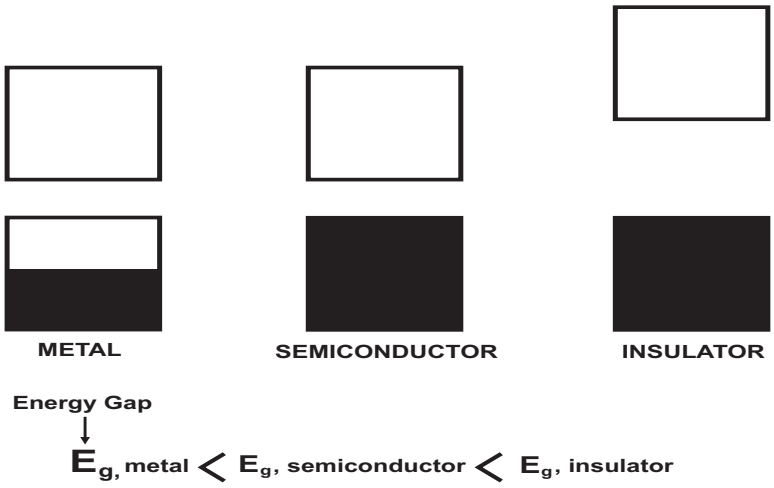

Figure 1.5: Band Gap Comparison [4]

An organic polymer that possesses the electrical, electronic, and optical properties of a metal while retaining the mechanical properties, processibility, etc. commonly associated with a conventional polymer, is termed an "intrinsically conducting polymer" (ICP) [5]. ICPs fall into the category of semiconductors due to the π-conjugation that occurs with their orbital shells. The overlapped π-bands are the valence bands and the π^* bands are the conduction bands [4].

A polymer can be made conductive by simply filling it up with conductive particles. This is termed "doping" and one can dope a polymer with metal or carbon filler. Doping a polymer gives an overall conductivity that is highly dependent on the particle size of the conducting filler and the distribution of the filler in the polymer matrix. Thus, there may be areas where the conduction of the doped polymer equals that of the base

polymer only and other areas where the conduction is as high as the filler itself! This inconsistency with conductivity motivated others to consider an inherently conductive polymer; e.g. one that has an isotropic conductivity.

Intrinsic conductivity of a polymer is a unique property of organic materials. Organic materials give rise to conductivity due to π-conjugation, the overlap of double bond orbitals in the polymer chain. ICPs differ from everyday polymers, such as polyethylene, polypropylene, polyvinyl chloride, etc., because of their unique π-electron properties [4]. ICPs have measurable and significant electrical conductivities at room temperature. Obtaining these polymers employs the mechanism or either step-growth or chain-growth polymerization with an additional step to incorporate the conductive species.

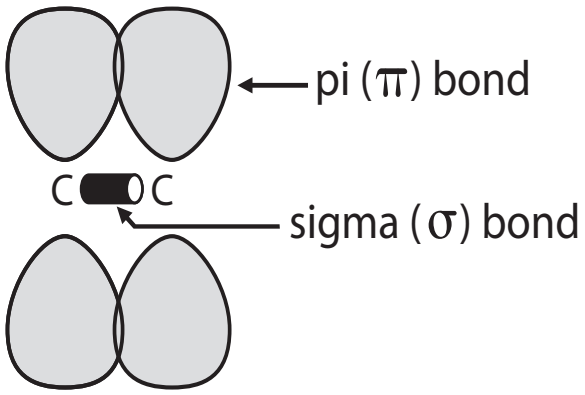

Figure 1.6: Sigma and Pi Bond [1]

All ICPs were made conductive through a doping process that is carried out via a chemical and/or electrochemical process [5]. It has been argued that the term "dopants" in this sense is incorrect. Being the anionic or cationic species impart an oxidized or reduced charge center in the polymeric backbone of the ICP, rather than an additive placed between polymer chains.

Chemical or electrochemical p-doping is accomplished by exposing the ICP to a solution or vapor of the dopant. This process creates a delocalized positive soliton across a portion of the C-H units.

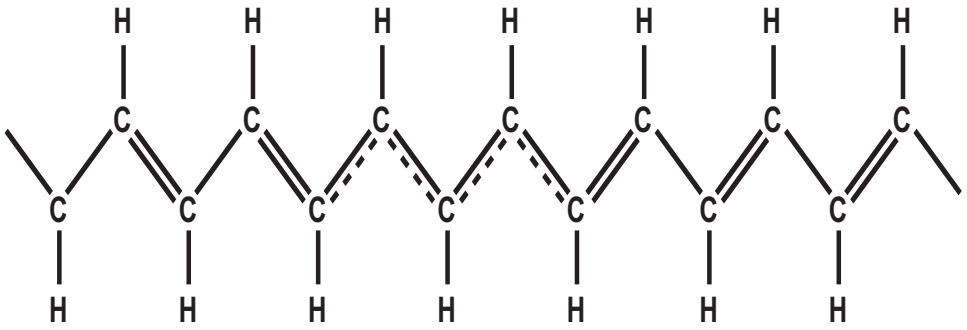

Figure 1.7: Soliton Creation

The creation of delocalized positive solitons in the backbone of a polymer chain.

Obtaining n-doped ICPs involves subjecting the ICP to an applied potential in a solution.

In all p- and n-doping processes, counter ions are formed which stabilize the charge on the polymer backbone [5]. These counter ions are termed solitons, polarons, bipolarons, etc. and each are formed on specific polymers and can be used as "spectroscopic signatures."

In this thesis, polyaniline (PANI) is the ICP of interest. To synthesize PANI, aniline liquid is mixed with an oxidant solution. The solution is then cooled to a temperature of $0°C$ while being stirred. The polymer obtained is then washed with a hydroxide solution and then dried. The resultant polymer contains overlapping π-bands, which lead to its inherent conductivity.

Notice in Figure 1.4 there is a separation between the overlapping *pi*-bands. These are the band gaps that are inherent to ICPs. Because there is a physical gap the electrons must overcome for conduction, ICP conduction is dependent on temperature and pressure changes.

Consider a matrix of ICP polymer chains. The chains are spaced somewhat apart from each other in an entangled arrangement. As pressure is applied to the chains, one can imagine the chains coming in closer proximity to each other. This changes the band gap scenario by decreasing the gap length or potentially eliminating it altogether. Thus

the ICP will have increased conductivity reaching values similar to that of metals! This phenomena has been reported by Bao and others [6].

1.3 Hardness Testing

When defining hardness, it is important to consider the audience. Hardness is a term that has different meanings to different people: to metallurgist it means resistance to indentation or penetration, to a tribologist it means resistance to wear, to a material scientist or design engineer it means a measure of flow stress, to a mineralogist it means resistance to scratching, and to a machinist it means resistance to cutting [7] [8] [1]. These definitions of hardness all converge to one underlying phenomena; the plastic flow stress of a material.

Measuring the hardness of a material involves choosing a measurement technique from a wide variety of choices. The measurement techniques range from macrohardness, microhardness and nanohardness scales. This range is indicative of both the size of the indenter and the amount of load (both of which reduce when going from macrohardness to microhardness to nanohardness). To appropriately choose a technique, we must first understand each technique and their respective applications and limitations.

1.3.1 Macrohardness

Macrohardness refers to applied loads on the indenter of more than 1 kg and covers the testing of tools, dies, and heavier gauge sheet materials [9]. Macromechanics of composites involves a volume element on the order of millimeters and above [10].

Macrohardness testing is a method employed to determine bulk hardness properties of a material. The method uses high loads and large indenters, comparatively. There are many types of macrohardness tests used for measuring polymers. The three main types are Rockwell, Durometer, and Barcol hardness tests.

Rockwell hardness testing is the most common hardness test used to measure materials; widely employed when measuring hardness of metals. Its ease of use and fast data output, a value can be obtained in seconds, contribute to its popularity. Hardness values can be obtained from the hardest metals to rigid polymers through the use of different indenter heads. No optical measurements are required, as all hardness readings

are direct.

The method of operation involves the use of the Rockwell hardness tester. Test specimens are placed on a stage where a minor load is applied. The load is applied through the indenter tip, either a ball or a diamond shape, onto the test specimen and the dial is set to zero. This minor load application mitigates surface roughness effects and increases the testing accuracy. The major load is then applied for a duration, usually five to fifteen seconds, and then removed. Depending on the material type, and its mechanical response, the reading is read from the dial either immediately or up to fifteen seconds later.

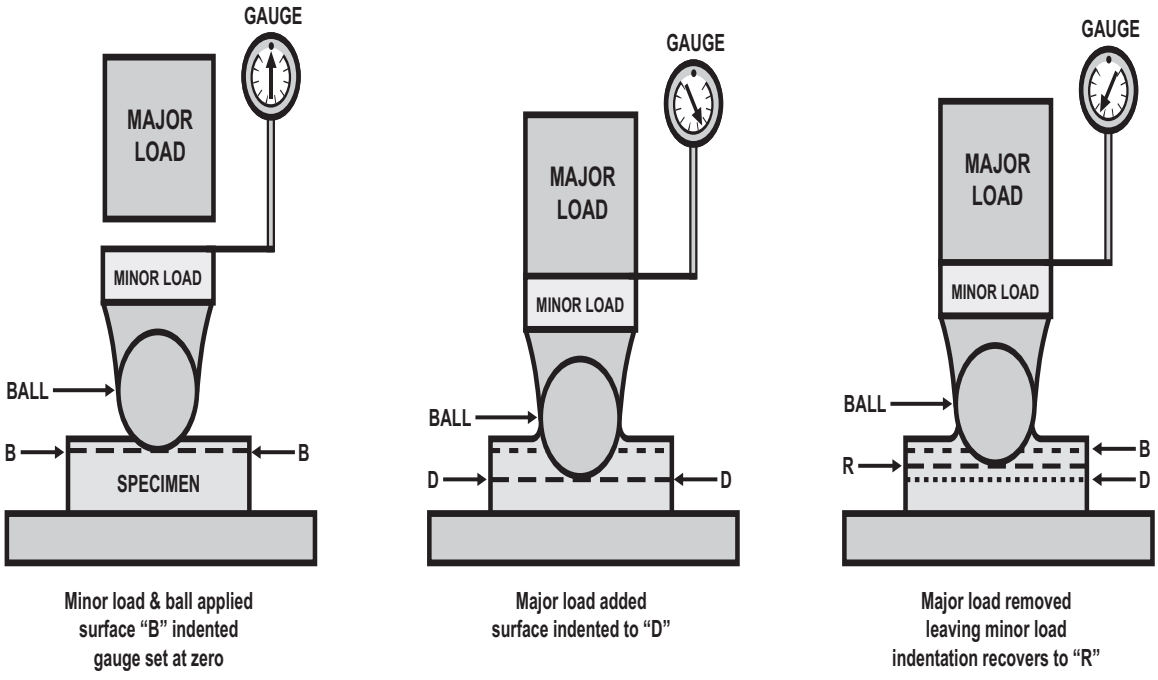

Figure 1.8: Rockwell Indentation [7]

Rockwell hardness of thermoplastic materials is measured in either the R or M scale. Thermosets, being typically stiffer with less creep, utilize a smaller indenter and a higher Rockwell scale of E. The table below shows the different Rockwell Hardness scales and their respective loads and indenter types.

Table 1.1: Table of Rockwell Hardness Scale [8]

Scale	Indenter	Minor Load $[kgf]$	Major Load $[kgf]$	Total Load $[kgf]$
A	Diamond Cone	10	50	60
B	$\frac{1}{16}$-inch Steel Ball	10	90	100
C	Diamond Cone	10	140	150
D	Diamond Cone	10	90	100
E	$\frac{1}{8}$-inch Steel Ball	10	90	100
F	$\frac{1}{16}$-inch Steel Ball	10	50	60
G	$\frac{1}{16}$-inch Steel Ball	10	140	150
H	$\frac{1}{8}$-inch Steel Ball	10	50	60
K	$\frac{1}{8}$-inch Steel Ball	10	140	150
L	$\frac{1}{4}$-inch Steel Ball	10	50	60
M	$\frac{1}{4}$-inch Steel Ball	10	90	100
P	$\frac{1}{4}$-inch Steel Ball	10	140	150
R	$\frac{1}{2}$-inch Steel Ball	10	50	60
S	$\frac{1}{2}$-inch Steel Ball	10	90	100
V	$\frac{1}{2}$-inch Steel Ball	10	140	150

The mechanical response of the material plays a role on the value of the Rockwell Hardness. Differences in elasticity, creep, and shear flow characteristics will change a materials response when recovering from the indenter load. With polymers, the more elastic the material the more recovery the plastic will have after the major load is removed. Thus the amount of time one takes prior to reading the gauge becomes significant to the hardness value. A more elastic polymer may give higher hardness values due to its memory properties.

1.3.2 Microhardness

The term microhardness usually refers to indentation hardness tests with loads not exceeding 1 kg [8] and is conducted on materials with thicknesses down to 0.0125 mm (or 0.0005 in) [9]. The micromechanics of a material covers a different spectrum than macromechanics as it constitutes at least one dimension in the micrometer range [10]

Microhardness tests differ from macrohardness tests also based on the change in shape of the indenter.

Microhardness can be measured with a Knoop or a Vickers indenter; Knoop is more popular in the United States whereas Vickers is more popular in Europe [8].

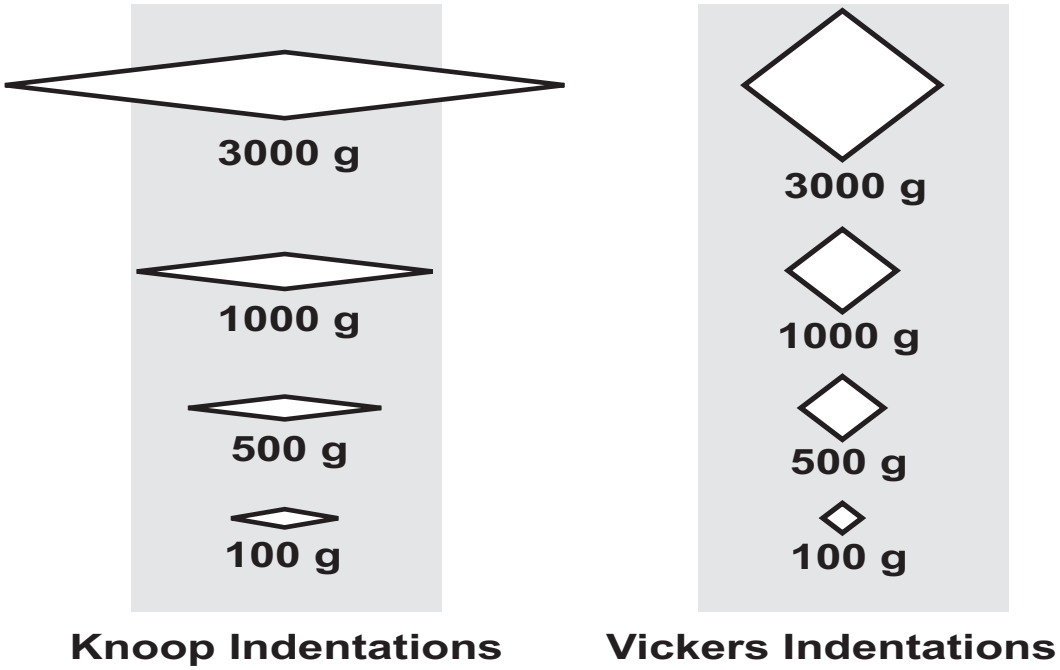

Figure 1.9: Knoop versus Vickers Indenter Tips [8]

Microhardness testing is performed via handheld or benchtop equipment. Loading is applied with a "dead load" and benchtop units are equipped with optical equipment (microscopes) for viewing of the indentation. Testing error include inaccuracy in loading, vibration, rate of load application, duration of contact period and impact [8].

Measuring the hardness of rigid thermoplastics; both reinforced and non-reinforced,

can also be done through the use of Barcol hardness testing. The Barcol hardness tester is a handheld that has a sharp, conical tip that penetrates into the surface of the material being tested. Hardness values are given on a dial face based on the depth of penetration. The dial has 100 divisions with each division representing a depth of 0.0003 inches. The ease of use, being handheld, and the ability to obtain quick numbers make Barcol hardness testing a popular method. However, the inconsistency in results due to application of load make it suspect to questions of accuracy and repeatability.

Improvements to hardness repeatability are obtained through the use of Durometer Hardness Testing. Durometer testing is similar in logic to Barcol testing. Both tests measure the of depth of tip penetration into a material. Durometer testing, however, employs the use of a bench top instrument (though handheld versions are also available) to aide in the repeatability and consistency of the application of the penetrating load. Hardness values are given in either the A or D scale; where the A scale is for soft materials and the D scale is for more rigid materials. The difference in the testing involves changes to the shape and dimension of the indenter.

The resulting measurement from Durometer testing gives a relative hardness number. Keep in mind that all hardness scale conversions are not precise, but are estimates. This is due to the fact that hardness numbers are based on empirical data. These hardness values can be related to Rockwell hardness based on the following scale:

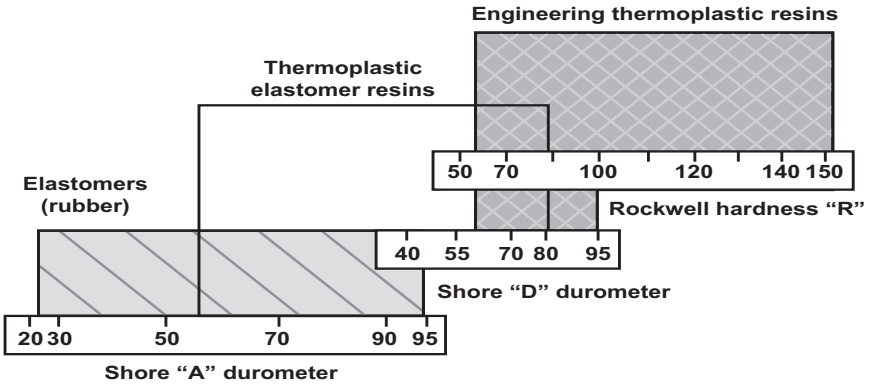

Figure 1.10: Hardness Comparison [7].

Determining the hardness value of a metal traditionally involves the use of imaging. The imaging involves a visual observation of the indent from which the contact area and hardness values can be calculated. This imaging technique is not suitable for obtaining elastic and elasto-plastic properties of materials. [11] Imaging is also not very useful when conducting micro or nanoindentation experiments, as the error in calculating the contact area can be quite large. Small scale indentation requires the use of a force-displacement curve during loading and unloading.

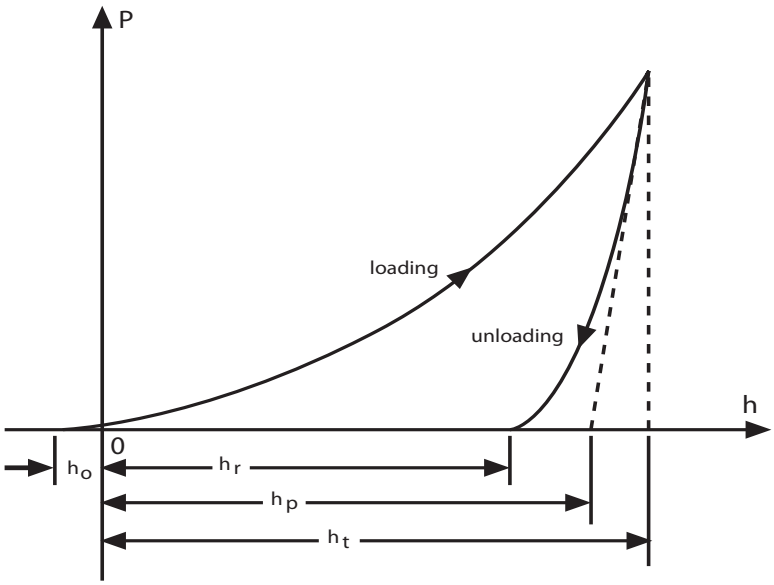

Figure 1.11: Load-Unload of PMMA [11]

Image detailing the load-unload force-displacement curve of a PMMA sample at $20°C$ *indented with a conical indenter* .

From the unloading curve above, the hardness and elastic modulus can be obtained through the use of a curve fitting procedure. The curve fitting is conducted using the Box-Cox transformation, which is of the form:

$$P = m(h - h_0)^n \tag{1.1}$$

where

P = indentation load,

n = index of deformation,

h_0 = is the zero error in the measured value of h,

$m = gE^*$,

g = a geometric factor,

E^* = reduced elastic modulus = $\frac{1-\nu_1^2}{E_1} + \frac{1-\nu_2^2}{E_2}$,

ν_1 = Poisson's ratio of the polymer,

ν_2 = Poisson's ratio of the indenter material,

E_1 = moduli of the polymer,

E_2 = moduli of the indenter material.

Assuming $E_2 \gg E_1$, we have
$E^* = \frac{1-\nu_1^2}{E_1}$.

Relating the reduced elastic modulus to contact stiffness near h_t, we have

$$\frac{\partial P}{\partial h} = S = 2E^* a$$

where

P = indenter load,

S = contact stiffness,

a = contact radius = $(h_p + \delta)\tan\theta$ (for a cones).

Thus, hardness is defined as:

$$H = \frac{P}{\pi a^2}$$

Microhardness of polymers is well documented and reveals how polymers, both amorphous and crystalline, respond to indenter depth.

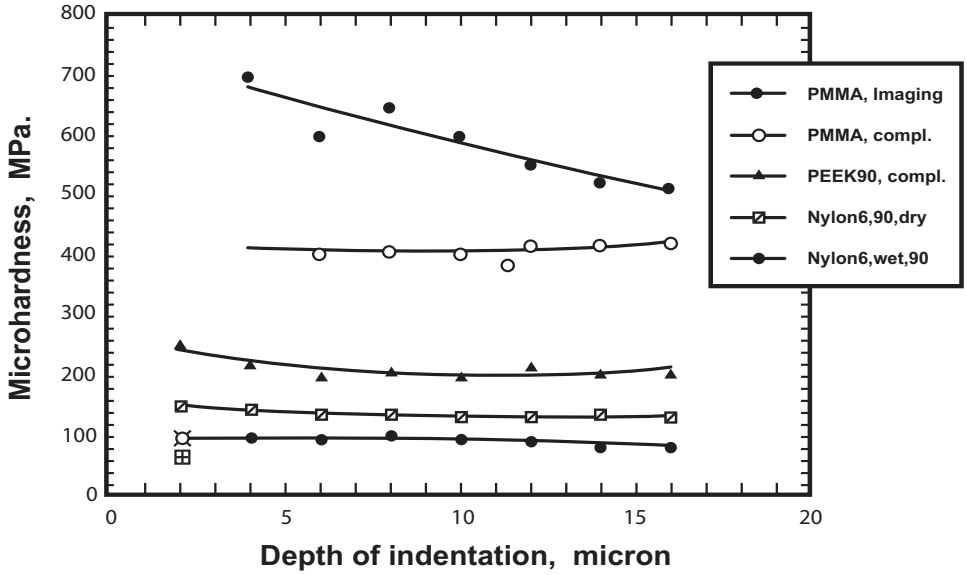

Figure 1.12: Microhardness versus Indentation Depth [11]

From the image above, we observe amorphous polymers (PMMA) do not show a dependence of hardness with the depth of indentation. Crystalline polymers have a small decrease in hardness with an increase in penetration depth. It is theorized this may be due to the presence of a transcrystalline layer on the exterior surface of the crystalline polymer [11].

Microhardness of polymers has a dependence on both intrinsic and extrinsic variables. Increases in polymer crystallinity increases hardness values. Parameters such as temperature, density and microstructure also effect the hardness values of polymers. Also, because of visco-elastic effects, time can contribute significantly to hardness values of polymers.

The microhardness values obtained for polymers have been shown to be linearly related to plastic yield stress. It has been shown that the ratio of hardness to plastic yield stress approaches three for crystalline polymers, as depicted below.

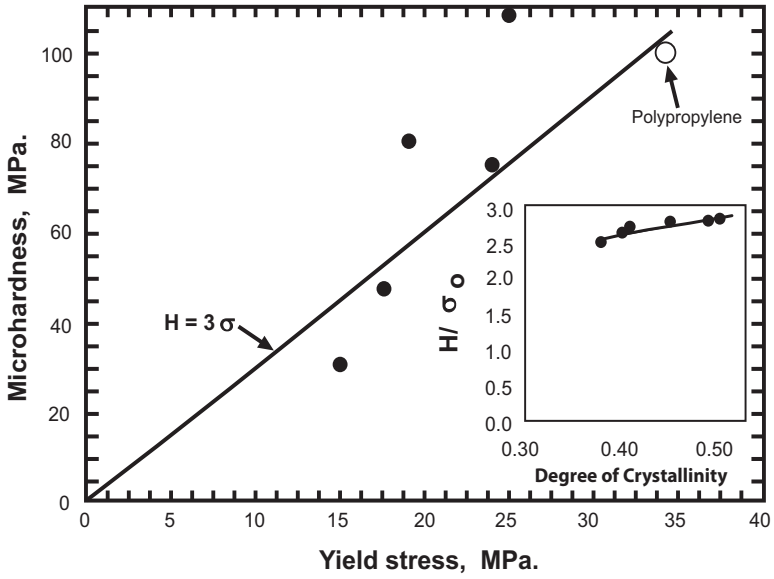

Figure 1.13: Microhardness versus Yield Stress [11]

1.3.3 Nanohardness

As mentioned above, when the scale of hardness decreases so do the forces and penetrations exhibited. With nanohardness testing, the forces involved are usually in the range of millinewton (10^{-3}) down to a few nanonewtons (10^{-9}) Similar ranges are found when consider depths [12]. Nanoindentation employs the fundamental principles of indentation loading based on research published by Hertz. In the case of nanomechanics, at least one dimension of the material should be on the nanoscale [10].

Consider the classic scenario between a rigid sphere and a flat surface.

Geometric illustration of a spherical contact and a flat specimen.

The mathematical relationship of the above figure was published by Hertz and is given by:

$$a^3 = \frac{3}{4}\frac{PR}{E^*} \tag{1.2}$$

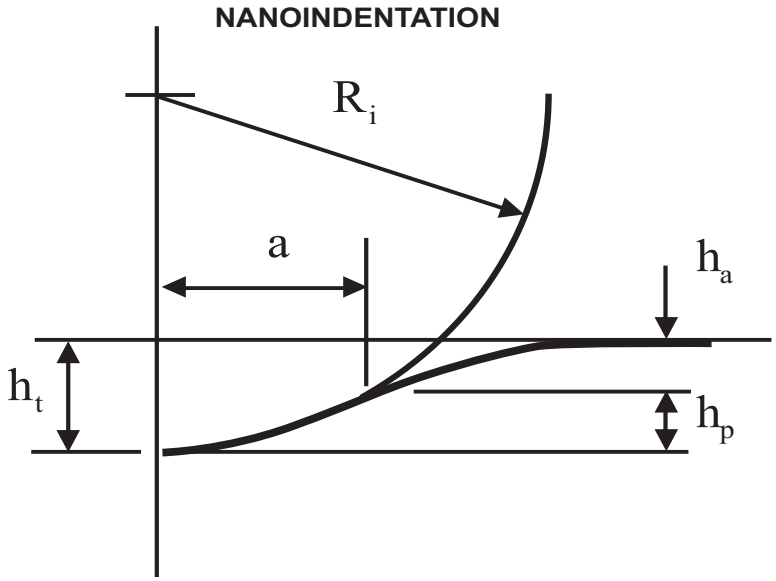

Figure 1.14: Sperical Contact [12]

where

a = radius of the circle of contact,

P = indenter load,

R = indenter radius,

E^* = reduced modulus.

The reduced modulus, E^*, combines the modulus of the indenter (1) and of the specimen (2). These elements have the following relation:

$$\frac{1}{E^*} = \frac{\left(1-\nu_1^2\right)}{E_1} + \frac{\left(1-\nu_2^2\right)}{E_2} \tag{1.3}$$

where

E = Young's Modulus,

$\nu = -\left|\frac{\epsilon_y}{\epsilon_x}\right| = -\left|\frac{\epsilon_z}{\epsilon_x}\right|$,

Poisson's ratio, ν, is the absolute value of the ratio of the lateral strain over the axial strain [13].

In the case where the contacting bodies both have curvature associated with them, the R in equation (1.2) is given by:

$$\frac{1}{R} = \frac{1}{R_1} + \frac{1}{R_2} \tag{1.4}$$

For the case of a rigid spherical indenter, the depth of the circle of contact beneath the specimen free surface is equal to exactly half of the total elastic displacement [12]. This is termed the *radius of contact* and is calculated from $h_a = h_p = h_t/2$.

The distance of mutual approach in the indenter and the specimen is given by $\delta = \delta_1 + \delta_2$. This occurs when both the indenter and the specimen undergo deformation.

$$\delta = \frac{a^2}{R} = \left[\left(\frac{3P}{eE^*} \right)^2 \frac{1}{R} \right]^{1/3} \tag{1.5}$$

In most cases, the deformation of the indenter is accounted for by E^*. Hence, the total depth of penetration h_t is equal to δ. Rearranging equation (1.5), we obtain:

$$P = \frac{4}{3} E^* R^{1/2} h_t^{3/2} \tag{1.6}$$

The applicable output of an indentation test is the indentation stress and indentation strain. These values are analogous to stress-strain relationships obtained in tensile and compression tests. The indentation stress-strain relationship reveals the elastic-plastic response of a material that is not obtainable via testing in tension or compression.

The mean contact pressure is the common term for the indentation stress and is given by:

$$p_m = \frac{P}{\pi a^2} \tag{1.7}$$

Combining equations (1.5), (1.6), and (1.7), we obtain:

$$p_m = \left(\frac{4E^*}{3\pi}\right)\frac{a}{R} \tag{1.8}$$

where the term $\frac{a}{R}$ is known as the indentation strain.

Chapter 2

Nanoindentation of Inherently Conductive Polymers (ICPs)

2.1 Evaluation Plan

The purpose of this experiment is to obtain and evaluate the nanoindentation properties of inherently conductive polyaniline (PANI) films.

The reason for the analysis is to better understand how the conductivity of PANI film changes with an increase in mean pressure applied during indentation. These results will help promote PANI's use in electromechanical and electroluminescent devices.

2.2 Polyaniline (PANI)

Polyaniline (PANI) is a conducting polymer that can be used in numerous applications [14]. Synthesis of PANI is performed by either an electrochemical process with aqueous or non-aqueous electrolytes, or through casting PANI solutions in appropriate solvents.

The PANI films in this study were synthesized with H_2SO_4 and HNO_3. The samples are partially oxidized emeraldine forms of PANI. Different acids yield different morphologies with the PANI films. SEM imaging of these PANI films have been documented [14] and reveal very different morphologies depending on the type of acid used. Fibrous and granular features are present in SEM images of PANI films.

To chemical synthesize the PANI samples, an aqueous solution $(NH_4)_2S_2O_8$ was added to aniline in the presence of various electrolytes, HNO_3 and H_2SO_4. During this process a precipitate was formed, which was removed by filtration. After washing the PANI sample numerous times with the electrolyte, it is then dried under vacuum. The resultant film is a partially oxidized emeraldine film.

The electrolyte is what gives PANI its conductivity. The presence of an acidic solution allows for the appropriate oxidation and reduction mechanisms to occur [15].

Density of PANI films is manipulated by varying aniline concentrations during synthesis (proportionally). It has been noted, by Zotti et al., that different acids used in PANI films affect the polymerization rate.

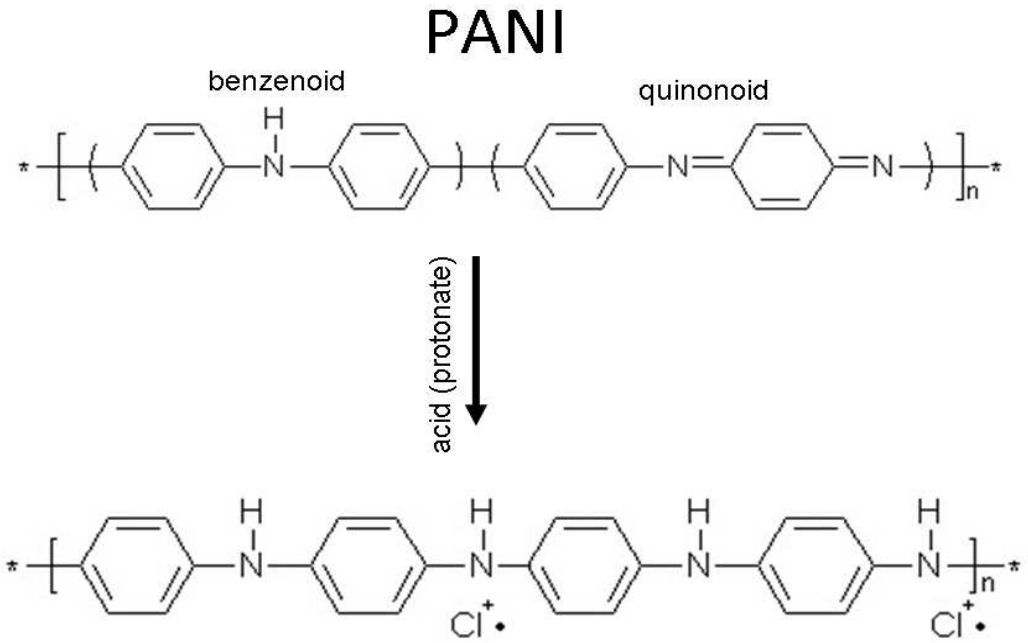

Figure 2.1: PANI Protonated with HCl

PANI films made from H_2SO_4 are much faster at polymerizing that HNO_3 films. It has been suspected that the increase in the charge to ion-size ratio of the anion has an effect on the polymerization rate. This leads to a theory that the anions are the rate-determining step of aniline polymerization in acidic solutions.

PANI emeraldine can be classified as a semicrystalline polymer [4]. Thus, at the nanoscale, these polymers are defined by lamellar crystals embedded with amorphous layers [10], which results in a high degree of anisotropy. Radial growth of these lamellae from a nucleation point form spherulitic textures. These spherulites have a complex microstructure and are generally classified to contain an isotropic spatial distribution of lamellae.

Under high deformation, the spherulitic structure is gradually broken down with a simultaneous increase in molecular orientation [10]. It has been shown, interestingly enough, that the spherulite size has little to no effect on mechanical properties of the polymer [16]. When the stress reaches a critical point, crystallographic slip takes control of the deformation process. Under plain strain, the plastic flow of the polymer ends quickly resulting in a straightening of the entangled chain network. The chain straightening results in strain hardening of the polymer. Little disentanglement occurs, which results in a very high stress value at low true strain.

The elastic properties of polymers are defined by the amount of crystalline and amorphous phases that are present. The crystalline phase consists of the polymer lamellae that have highly anisotropic behaviors and a very high modulus parallel to the polymer chain axis.

The amorphous phase, being confined between crystalline lamellae, has reduced chain mobility [17]. This mobility restriction reduces the molar mass and thus increases its modulus. The contribution of the modulus of the amorphous phase is greatly dependent on the evaluation temperature with respect to the glass transition temperature, T_g. If the experimental temperature is above the T_g, then one can assume the amorphous phase has no significant rigidity. The PANI in this study have a $T_g \simeq 30°C$. Therefore the tests were conducted at a temperature lower than their T_g.

At temperatures below the T_g, there is a very different physical effect that occurs. The interactions between the atoms occur at a much smaller scale and the elastic behavior of the amorphous phase is close to that of the bulk phase [10].

The utilization of carbon nanotubes as a filler in polymers has been of considerable interest from the academic community. This interest is derived from the following facts: they have high aspect ratios, exceptionally high stiffness, and have excellent electrical and thermal properties. Despite these advantages, poor dispersion and poor interfacial bonding limits their full utilization [10].

Single-wall carbon nanotubes (SWCNT) were employed in the samples of this study. They can be envisioned as graphene layers rolled into individual cylinders. These cylinders have a planar hexagonal arrangement of carbon-carbon bonds. The SWCNT were purchased and blended into the PANI films by Mohamoud A. Mohamoud [18]. Their diameters range from $1.2 - 1.5\ nm$ and their lengths range from $2 - 5\mu m$.

Proper dispersion into the PANI films is challenging due to the intrinsic van der Waals force between the nanotubes themselves. This force promotes the formation of nanotube clusters, which does not allow for homogeneous dispersion in the polymer film. This results in reduced mechanical performance of the film due to the inferior load transfer mechanism of the film. Dispersion of nanotubes can be improved through the use of chemical functional groups.

These functional groups allow for special reactions to occur between the treated nanotubes and the polymer itself. These reactions, such as etherification and amidization, improve interfacial bonding and homogeneous dispersion [10].

2.3 Technique and Setup

Nanoindentation evaluation of the polymer samples occurred at Hysitron [19]. The equipment used was a TI 900 TriboIndenter^{TM}. The TriboIndenter is a standalone nanomechanical characterization instrument that has many built-in features that allow for accurate measurement of both the load and displacement of the indentor tip. Many add-on features exist such as nanoDMA^{TM}, AFM imaging, Thermal Control, and nanoECR^{TM}. Three main objectives are met with the TriboIndenter: Software automation, environmental isolation, and transducer design.

2.3.1 Software Automation

Hysitron has developed a user-friendly software package that allows for automated acquisition of nanoindentation data. There are three types of control one can employ with the TriboIndenter: Open-Loop, Load Control, and Displacement Control.

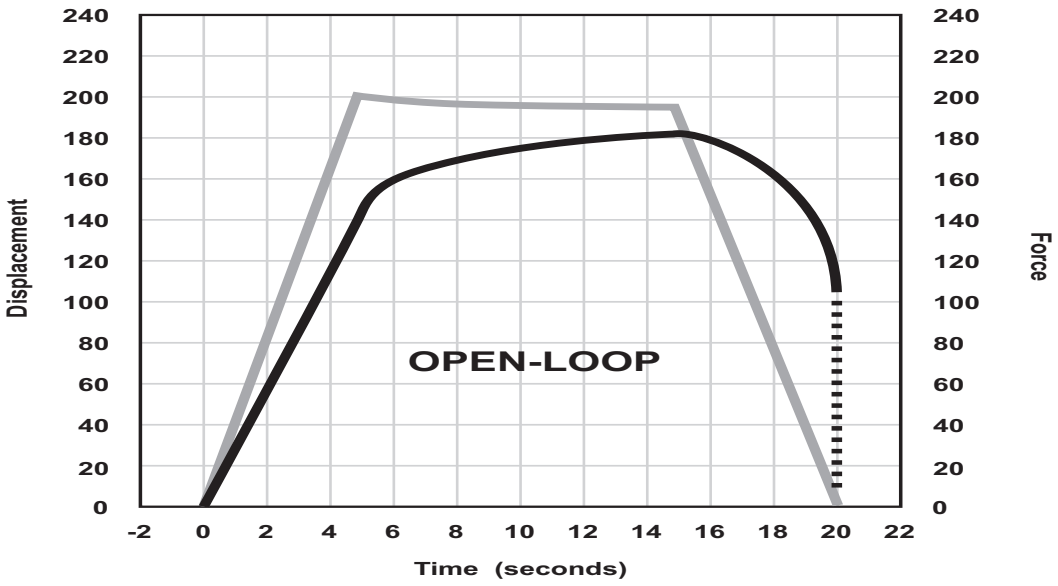

Figure 2.2: Open-loop Control [19]

Open-loop is the simplest control mechanism. There is no feedback, yet a maximum load and target loading rate is set for the indent experiment.

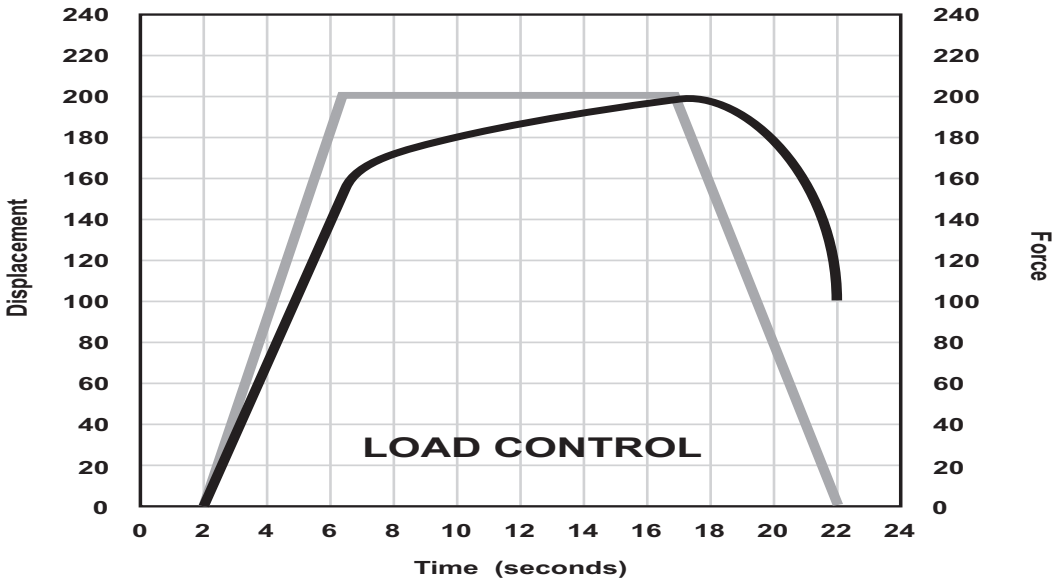

Figure 2.3: Load Control [19]

Load Control indentation testing utilizes a feedback control on both the loading rate and the maximum load. This type of control can be used to observe the relaxation behavior of visco-elastic materials.

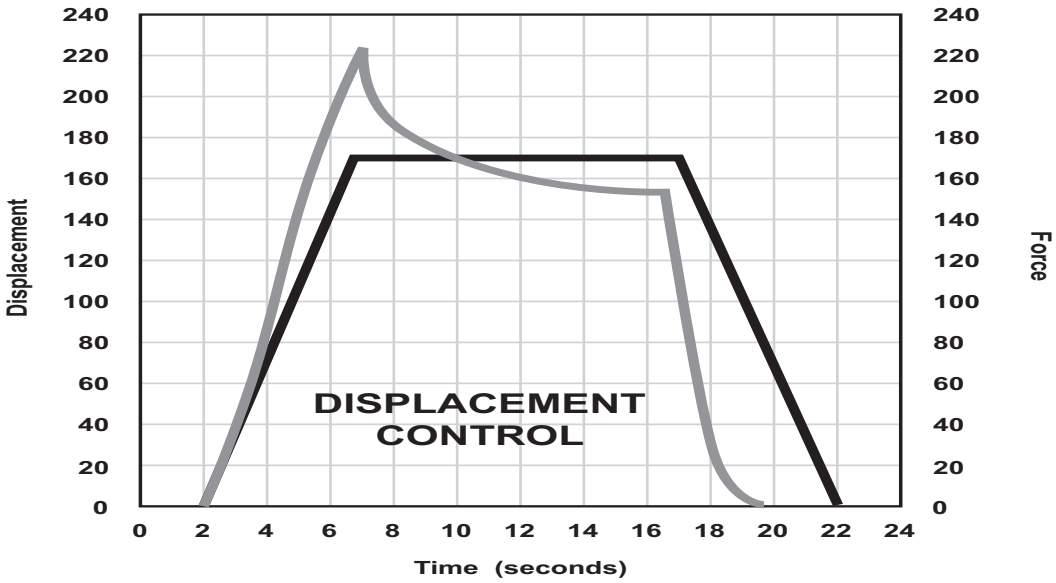

Figure 2.4: Displacement Control [19]

Displacement Control applies feedback to achieve target depth and displacement rate. This type of control is valuable when evaluating creep behavior of polymers or other visco-elastic materials.

2.3.2 Environmental Isolation

Vibrations of any type, e.g. acoustic noise, air currents, temperature gradients, mechanical vibrations, are detrimental to any nanoscale testing. The TriboIndenter is fitted with an engineered instrument enclosure designed to minimize vibration. The enclosure consists of double-walled fiberglass encapsulated with insulation layers. Additional dampening is obtained through the use of piezoelectric anti-vibrational stages. The combination of vibrational controls actively dampens vibrations under 200 Hz and passively dampens those over 200 Hz.

2.3.3 Transducer Design

The TriboIndenter employs a patented three-plate capacitive transducer. The technology allows the application of the force to be applied electrostatically and the transducer displacement is measured capacitively. This design works by applying AC signals

180° out-of-phase with each other to the top and bottom plate of the three-plate capacitive transducer. The middle plate, which is floating, cumulatively collects the signals from the top and bottom plate. This sum corresponds to a displacement of the plate. Applying a load involves the application of a DC voltage applied to the lower plate, which correspondingly electrostatically attracts the middle plate downward.

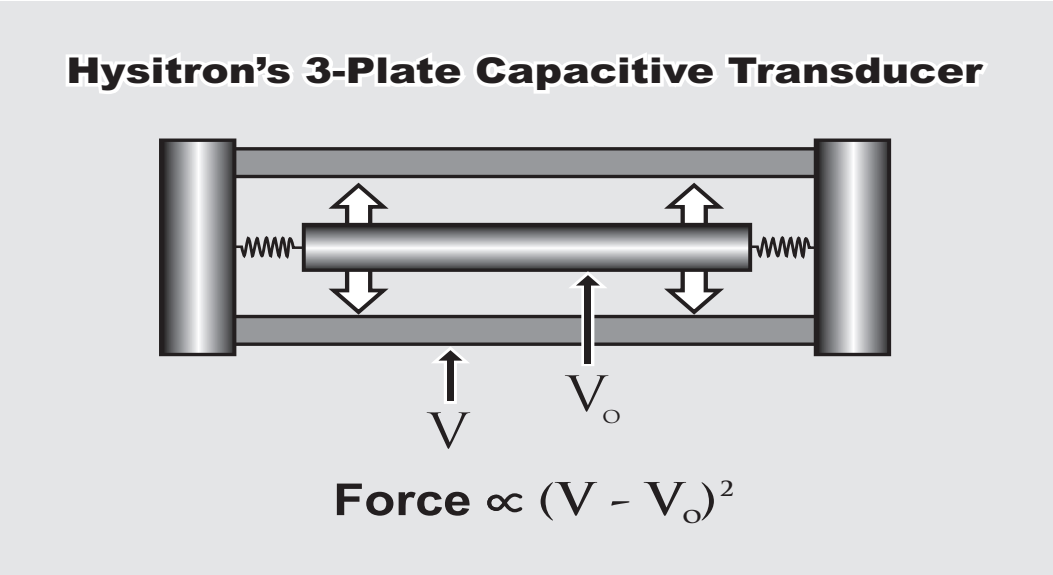

Figure 2.5: 3-Plate Capacitive Transducer [19]

The use of electrostatic actuation creates a lower heat scenario which reduces the occurrence of thermal drift. Thermal drift is a significant challenge to obtaining repeatable and meaningful data on the nanoscale. Mitigation of thermal drift is desirable because it creates a highly non-linear interference in the data that cannot be mathematically corrected. Therefore, the use of a low heat generating technique, like electrostatics, is a preferential method when conducting nanoindentation experiments.

2.3.4 nanoECR^{TM}

The TriboIndenter^{t}*extregistered* testing system has an add-on option for evaluating conductivity of a sample. This add-on is termed nanoECR^{TM} and combines the use of a conductive probe, a Keithley source multimeter, and a data acquisition card. The setup

of the samples on the indenter stage involves the series of resistivities from the following items; boron doped diamond (BDD) tip (R_{BDD}) the sample being tested (R_{film}) the internal instrument wiring (R_{int}) the bonding agent (R_{BA}) and the copper mounting surface (R_{Cu}).

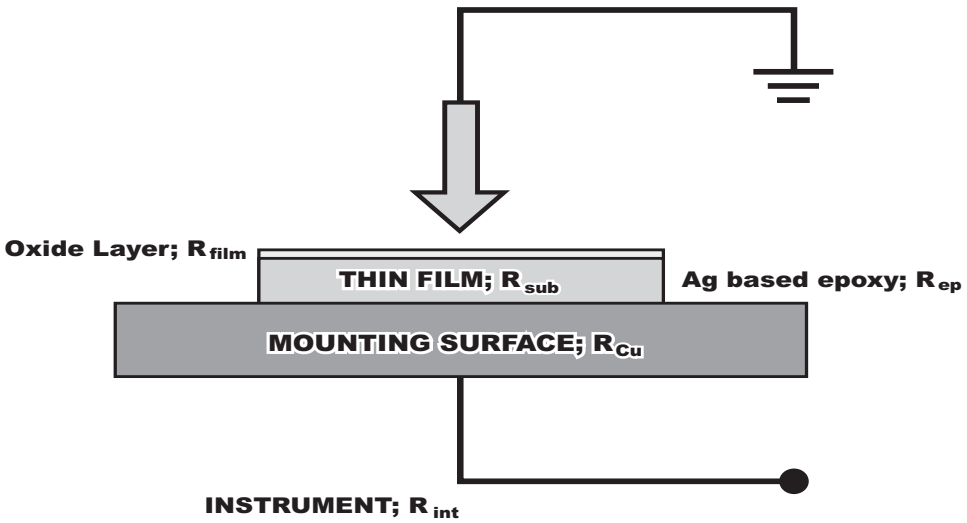

$$R = \sum_{i=1}^{n} R_i = R_{\text{int}} + R_{Cu} + R_{film} + R_{BDD} + R_{ep} + R_{sub}$$

Figure 2.6: Resistivity Schematic of Hysitron nanoECR Unit [20]

The Keithley source meter supplies both a current or voltage bias transmitted by the data acquisition card in the TriboIndenter. The data is averaged over a finite time period and stored in a bijective relationship to time, load, and displacement.

2.3.5 Experimental Parameters

The loading function used in this study consists of three segments. The first segment is the loading part with a constant rate of 20 $\mu N/s$ held for three seconds. The middle segment is at a fixed max load. The third and final segment is the unloading portion with the same rate as the loading portion.

All samples were prepared through the efforts of Mohamoud A. Mohamoud with the Department of Chemistry, University of Leicester, U.K.. Mohamoud synthesized polyaniline, abbreviated as PANI, samples grown from electrolyte of two types of acids, sulfuric acid and nitric acid. Single wall carbon nano-tubes (SWCNT) were also incorporated into some of the films to see what effect they would have on the film properties, mechanical and electrical.

The samples were as follows:

1-a PANI grown from electrolyte containing H_2SO_4,

1-b Same as 1-a with 20 $wt\%$ SWCNT,

2-a PANI grown from electrolyte containing HNO_3,

2-b Same as 1-b with 20 $wt\%$ SWCNT.

The films were applied to a soda-lime glass slide. During nanoindentation testing, the following stage map was used:

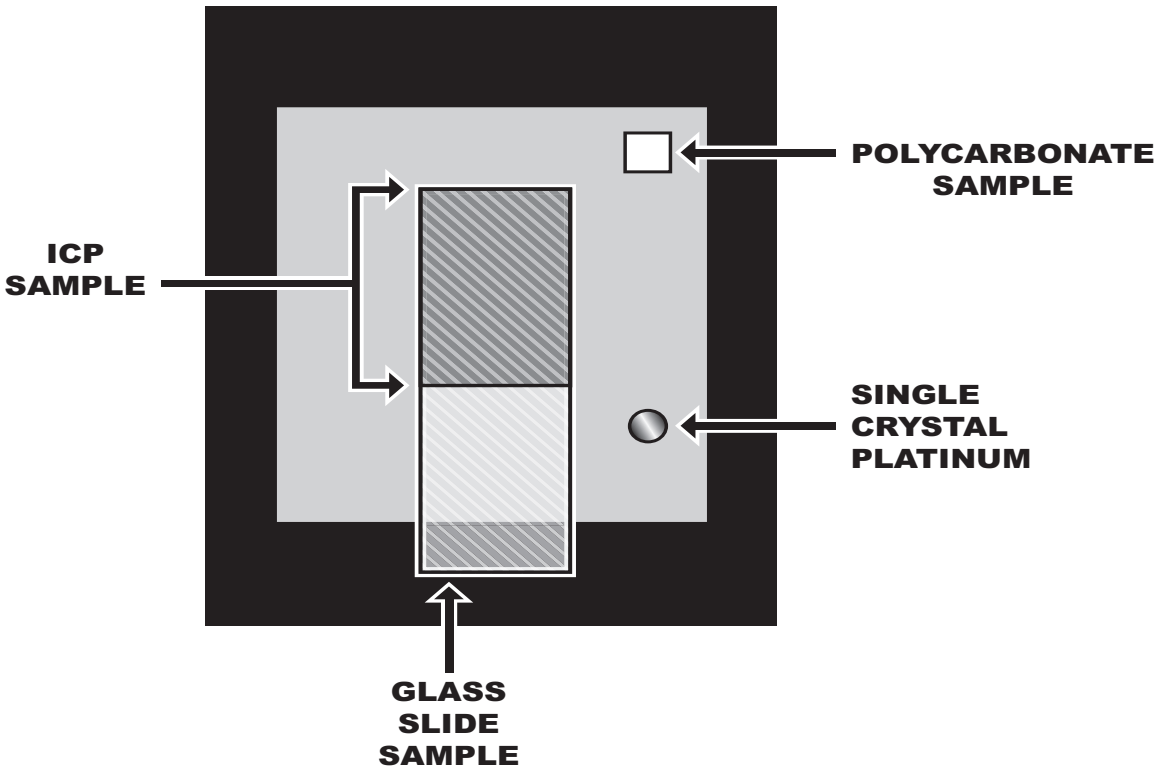

Figure 2.7: Nanoindentation Stage Map [20]

The stage contained two other materials that were tested at each step: a non-conducting polymer (PC) and a conducting metal (Pt). Prior to testing each sample, the PC was tested to ensure the indenter tip was measuring applied force and Pt was tested to ensure the indenter tip was measuring conductance (Pt).

The tip used was a 800 Berkovich tip (TB11231). This tip, in combination with the nanoECR^{TM}, allowed for conductivity measurements of the polymer samples. This tip is a single crystal boron doped diamond indenter. The result is a boron doped diamond (BDD) tip with a nominal resistivity of 3.3 $\Omega \cdot cm$ [20].

The loading and unloading rate remained the same for all samples tested in this study. The max loading was varied from 25 μN up to 150 μN to obtain a spread of data for understanding how the thin film responded to higher forces. Data was collected over a period of three months.

Chapter 3

Experimental Results

Referring to the image of the experimental stage setup, the results of the nanoindentation experiments are as follows.

We will analyze the results in groupings of two. Each grouping will compare the PANI samples with and without SWCNT at the same loading.

3.1 PANI + H_2SO_4

These graphs show PANI grown with H_2SO_4. The figures labeled with a are the neat polymer. The figures labeled b are the neat polymer with SWCNT.

For a spherical indenter, the radius of the circle of contact is given by:

$$a = \sqrt{2R\delta - \delta^2} \tag{3.1}$$

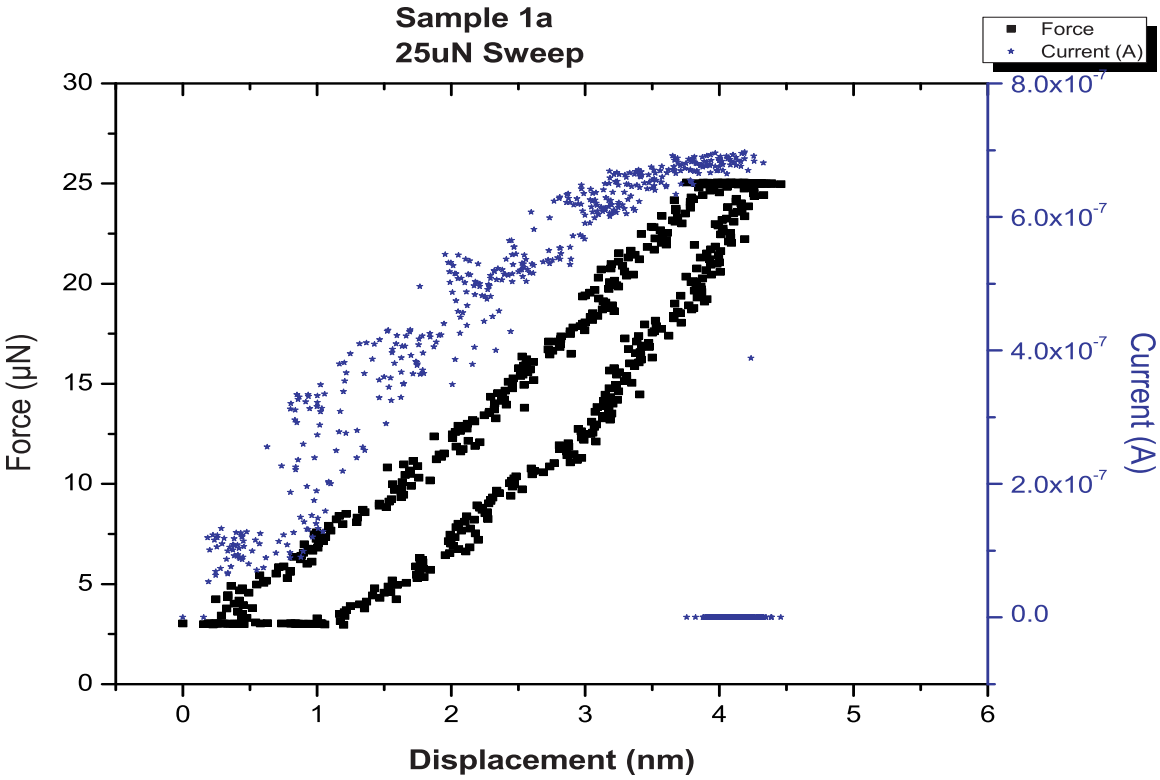

Figure 3.1: Graphical result - Sample 1a, 25uN

Graphical result of PANI sample grown from H_2SO_4 with a max indenter load of $25\mu N$.

From this plot, at $F = 25\ \mu N$ the displacement δ is 3.9 nm.

Given $R \simeq 800\ nm$, we have:

$a = \sqrt{2(800\ nm)(3.9\ nm) - (3.9\ nm)^2}$

implying $a \simeq 78.9\ nm$.

Using equation (2.7), we obtain the mean pressure for sample a at $25\mu N$:

$p_{m,25_{1a}} = \frac{25\mu N}{(78.9nm)^2\pi}$

and hence $p_{m,25_{1a}} \simeq 1.28\ GPa$.

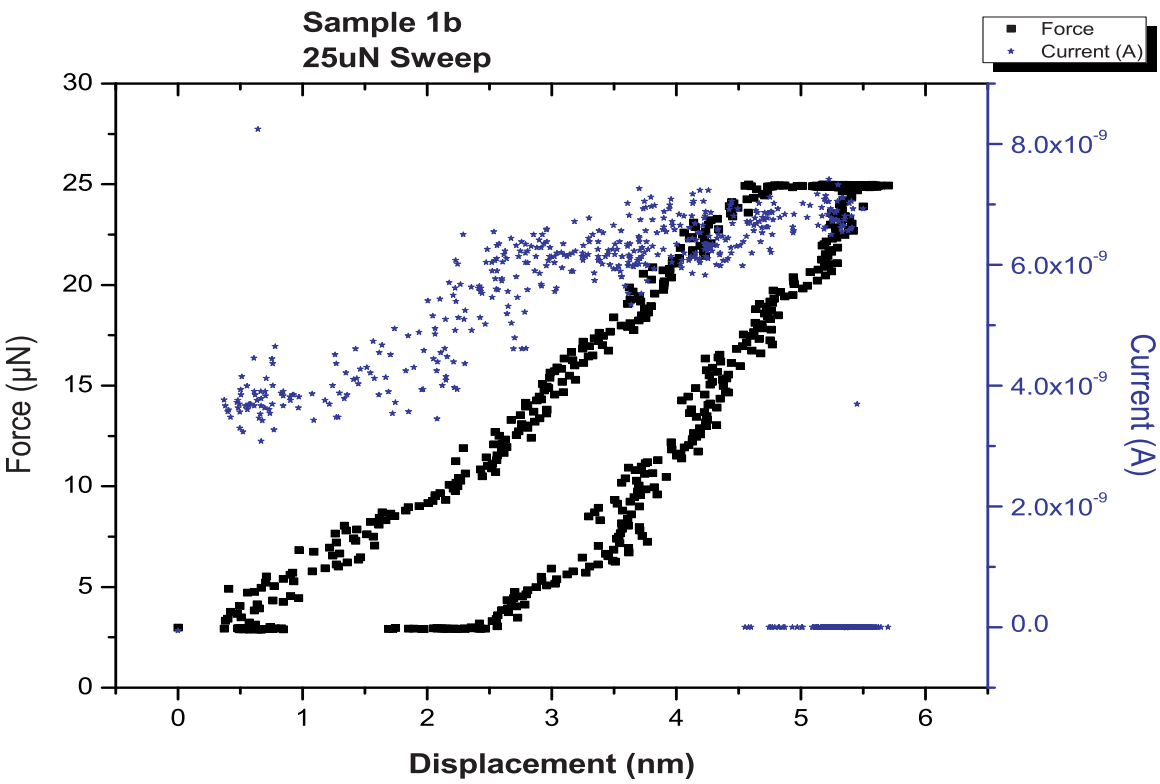

Figure 3.2: Graphical result - Sample 1b, 25uN

Data plot of PANI sample grown from H_2SO_4 *plus* 20 *wt% SWCNT with a max indenter load of* $25\mu N$.

we have $F = 25\ \mu N$ and $\delta = 4.75\ nm$, we conclude that
$a \simeq 87.0\ nm$,
and $p_{m,25_{1b}} \simeq 1.05\ MPa$.

Notice the depth of penetration is deeper in the SWCNT sample. Also, the conductance is markably less with SWCNT.

It's possible the distribution of SWCNT created voids in the microstructure. These voids would cause a reduction in conductance along with a deeper penetration at the same loading.

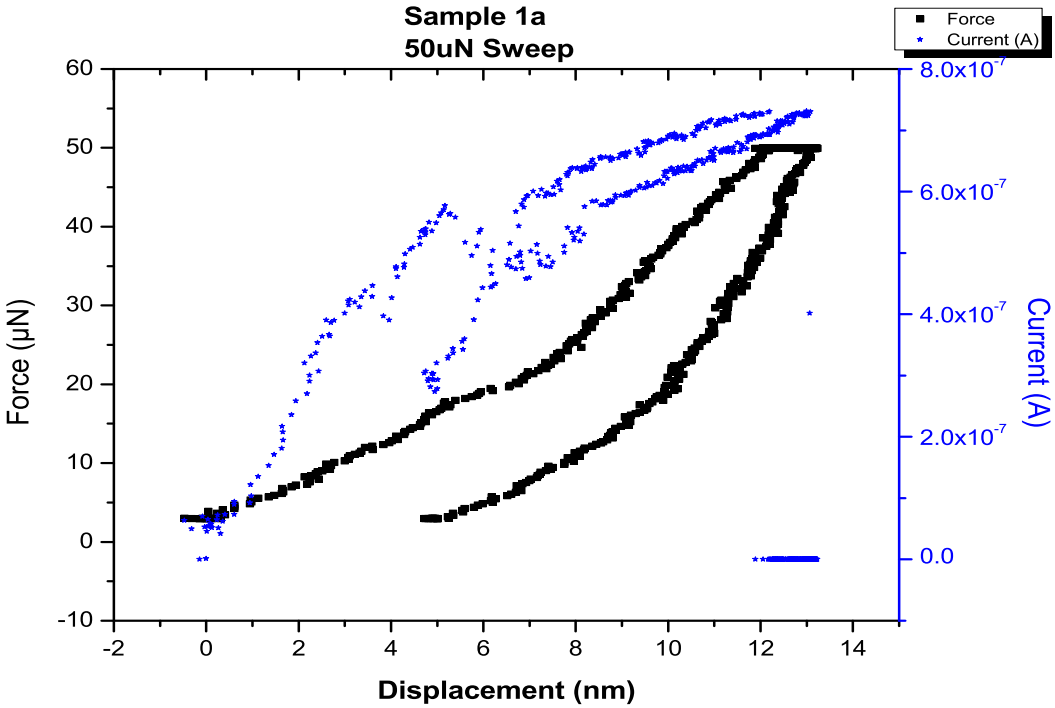

Figure 3.3: Graphical result - Sample 1a, 50uN

Data plot of PANI sample grown from H_2SO_4 *with a max indenter load of* $50\mu N$.

we have $F = 50\ \mu N$ and $\delta = 12\ nm$, we conclude that
$a \simeq 138\ nm$,
and $p_{m,50_{1a}} \simeq 835\ MPa$.

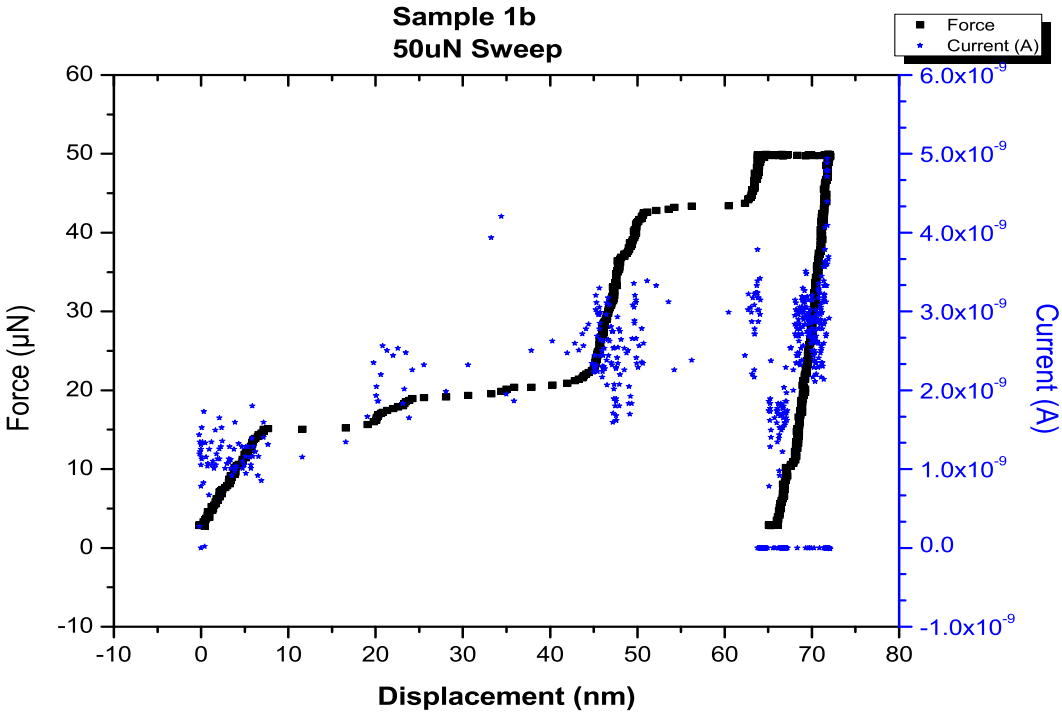

Figure 3.4: Graphical result - Sample 1b, 50uN

Data plot of PANI sample grown from H_2SO_4 *plus* 20 *wt% SWCNT with a max indenter load of* $50\mu N$.

we have $F = 50\ \mu N$ and $\delta = 65\ nm$, we conclude that
$a \simeq 449\ nm$,
and $p_{m,50_{1b}} \simeq 78.9\ MPa$.

The depth of penetration is much greater in the SWCNT sample. Also, the same decrease in conductance is evident in the SWCNT sample as compared to the neat polymer.

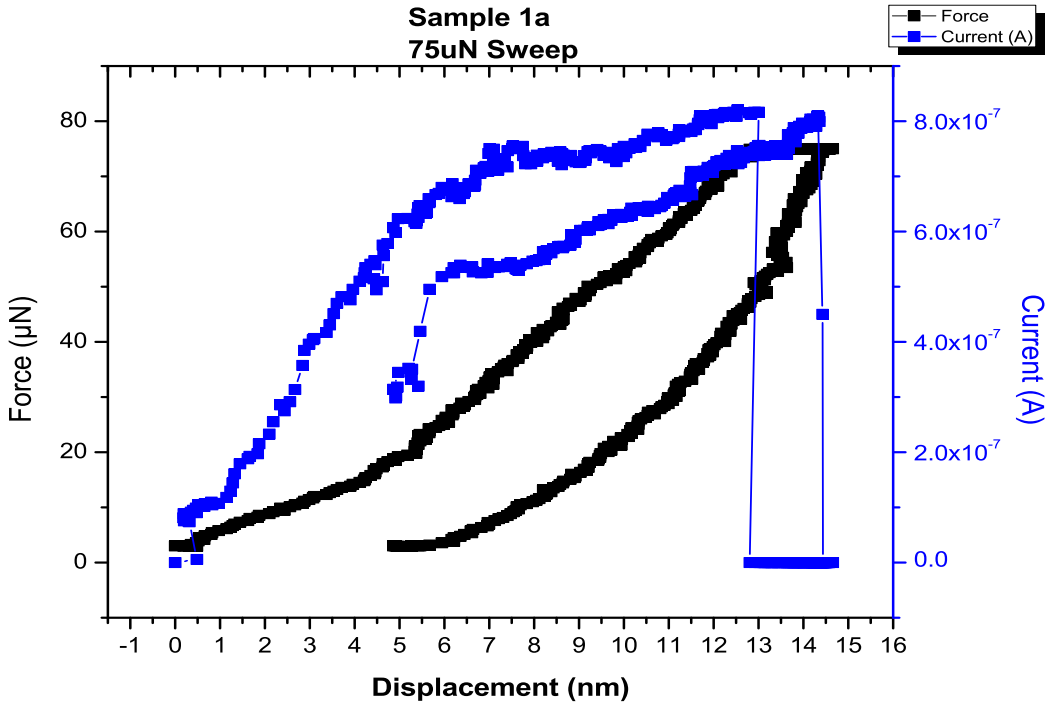

Figure 3.5: Graphical result - Sample 1a, 75uN

Data plot of PANI sample grown from H_2SO_4 with a max indenter load of $75\mu N$.

we have $F = 75\ \mu N$ and $\delta = 13\ nm$, we conclude that
$a \simeq 144\ nm$,
and $p_{m,75_{1a}} \simeq 1.16\ GPa$.

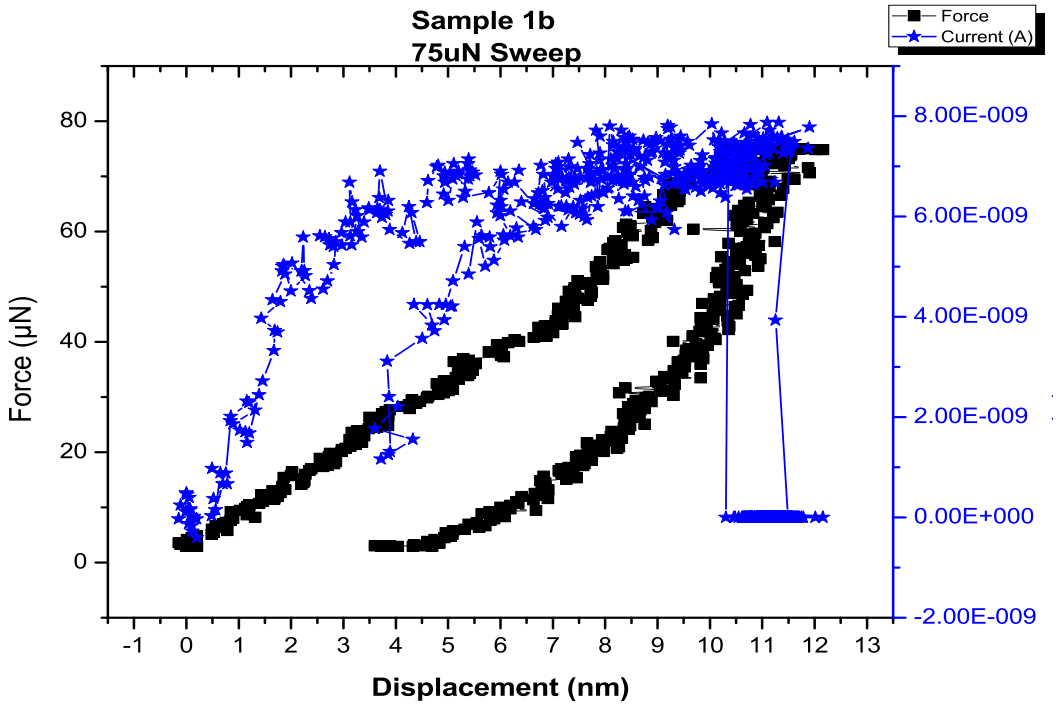

Figure 3.6: Graphical result - Sample 1b, 75uN

Data plot of PANI sample grown from H_2SO_4 *plus* 20 *wt% SWCNT with a max indenter load of* $75\mu N$.

we have $F = 75\ \mu N$ and $\delta = 11\ nm$, we conclude that
$a \simeq 132\ nm$,
and $p_{m,75_{1b}} \simeq 1.37\ GPa$.

In these two plots, the depth of penetration is nearly the same. Yet, the conductance is much less with the SWCNT.

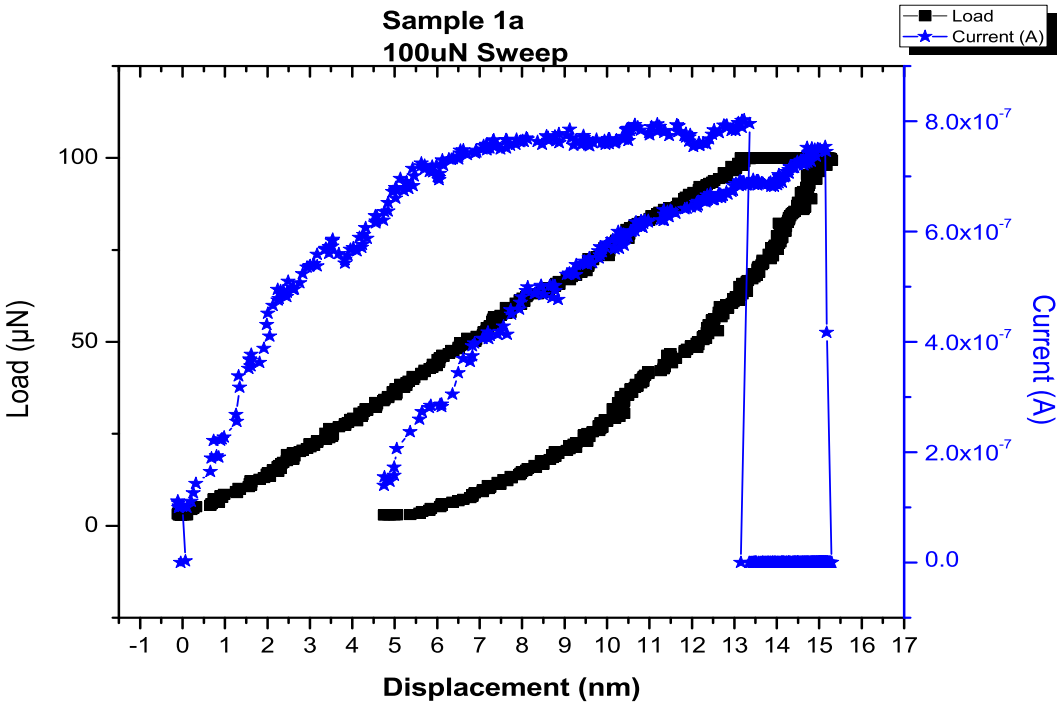

Figure 3.7: Graphical result - Sample 1a, 100uN

Data plot of PANI sample grown from H_2SO_4 *with a max indenter load of* $100\mu N$.

we have $F = 100\ \mu N$ and $\delta = 13\ nm$, we conclude that
$a \simeq 144\ nm$,
and $p_{m,100_{1a}} \simeq 1.54\ GPa$.

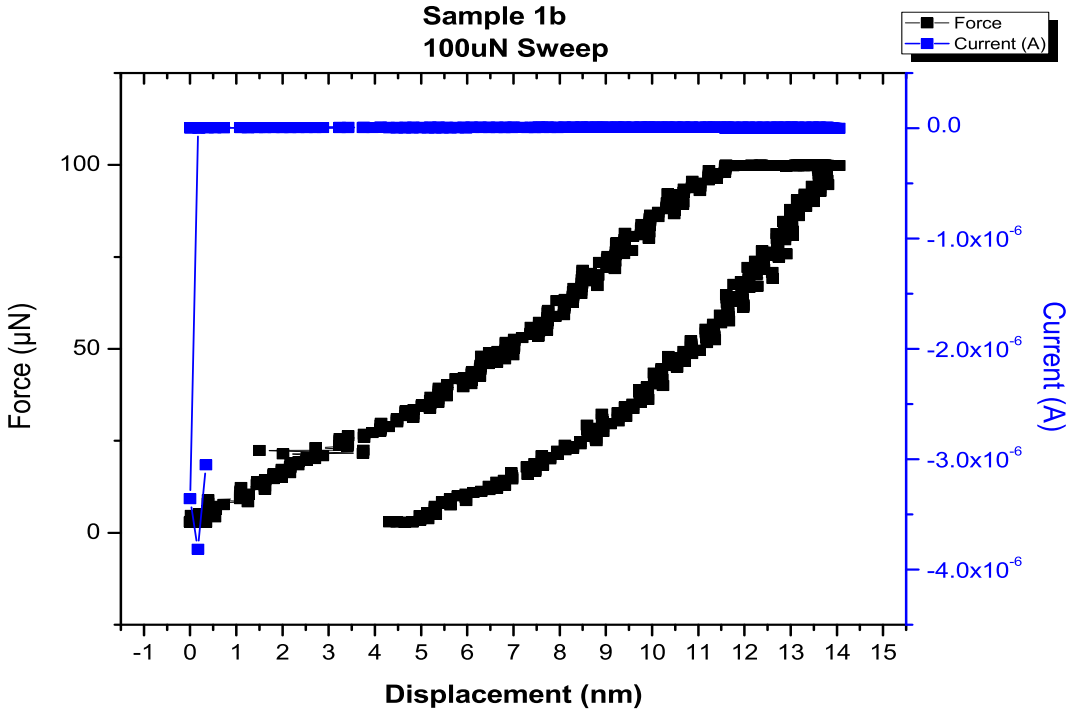

Figure 3.8: Graphical result - Sample 1b, 100uN

Data plot of PANI sample grown from H_2SO_4 *plus* 20 *wt% SWCNT with a max indenter load of* $100\mu N$*. NOTE: No current reading due to equipment malfunction.*

we have $F = 100\ \mu N$ and $\delta = 11.5\ nm$, we conclude that
$a \simeq 135\ nm$,
and $p_{m,100_{1B}} \simeq 1.74\ GPa$.

The depth of penetration is nearly equivalent, yet the conductance was not measured in the SWCNT sample.

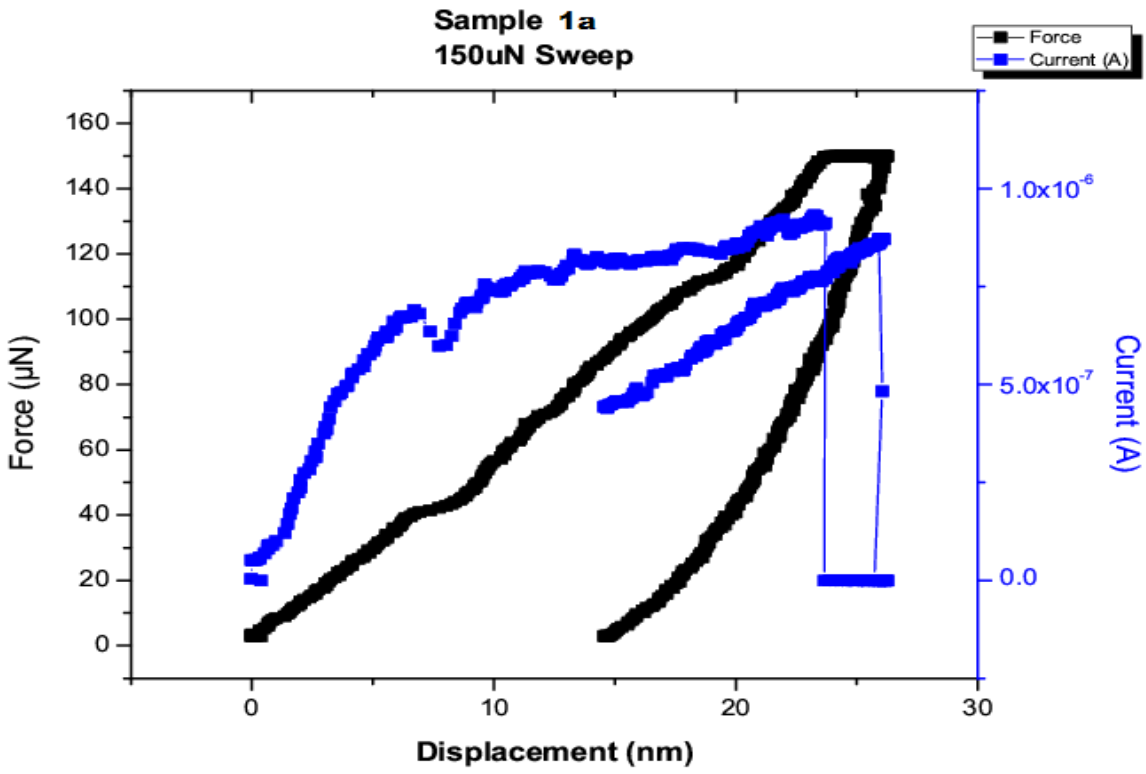

Figure 3.9: Graphical result - Sample 1a, 150uN

Data plot of PANI sample grown from H_2SO_4 *with a max indenter load of* $150\mu N$.

we have $F = 150\ \mu N$ and $\delta = 23\ nm$, we conclude that
$a \simeq 190\ nm$,
and $p_{m,150_{1a}} \simeq 1.32\ GPa$.

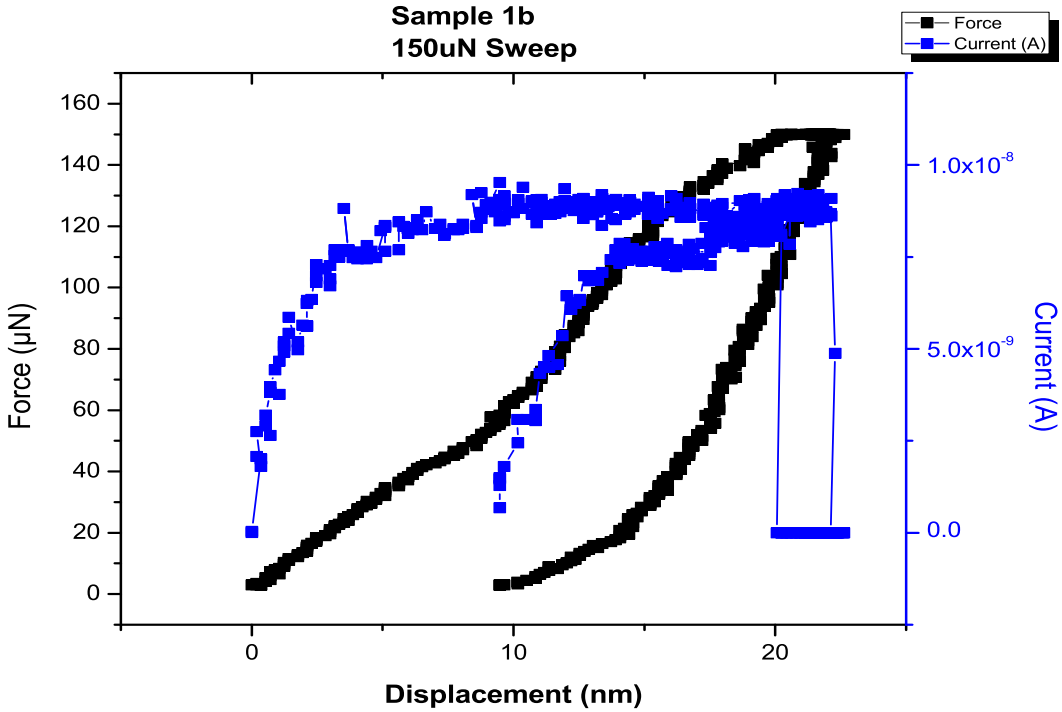

Figure 3.10: Graphical result - Sample 1b, 150uN

Data plot of PANI sample grown from H_2SO_4 *plus* 20 *wt% SWCNT with a max indenter load of* $150\mu N$.

we have $F = 150\ \mu N$ and $\delta = 20\ nm$, we conclude that
$a \simeq 178\ nm$,
and $p_{m,150_{1b}} \simeq 1.51\ GPa$.

The depth of penetration is greater in the neat polymer. The decrease in conductance is still evident in the SWCNT sample.

3.2 PANI + HNO_3

These samples are PANI samples grown from HNO_3. The samples labeled a are the neat polymer, whereas the sample labeled b are the neat polymer plus SWCNT.

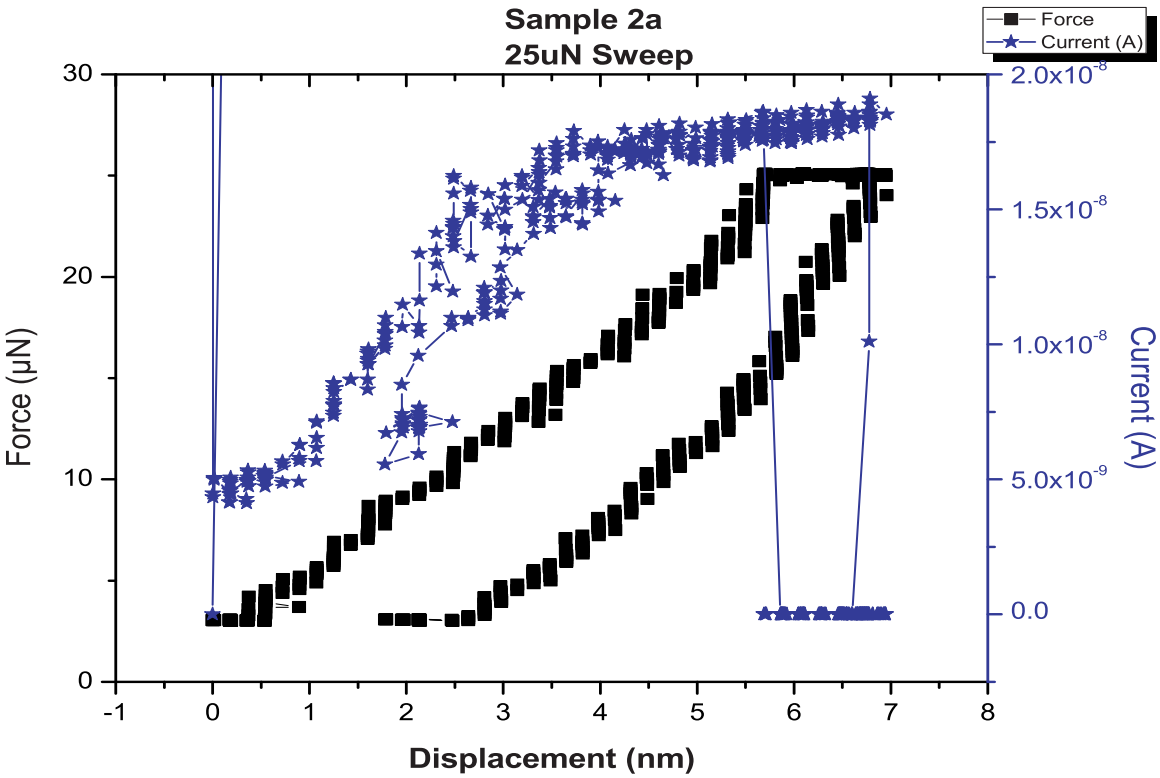

Figure 3.11: Graphical result - Sample 2a, 25uN

Data plot of PANI sample grown from HNO_3 with a max indenter load of $25\mu N$.

we have $F = 25\ \mu N$ and $\delta = 5.5\ nm$, we conclude that
$a \simeq 93.6\ nm$,
and $p_{m,25_{2a}} \simeq 907\ MPa$.

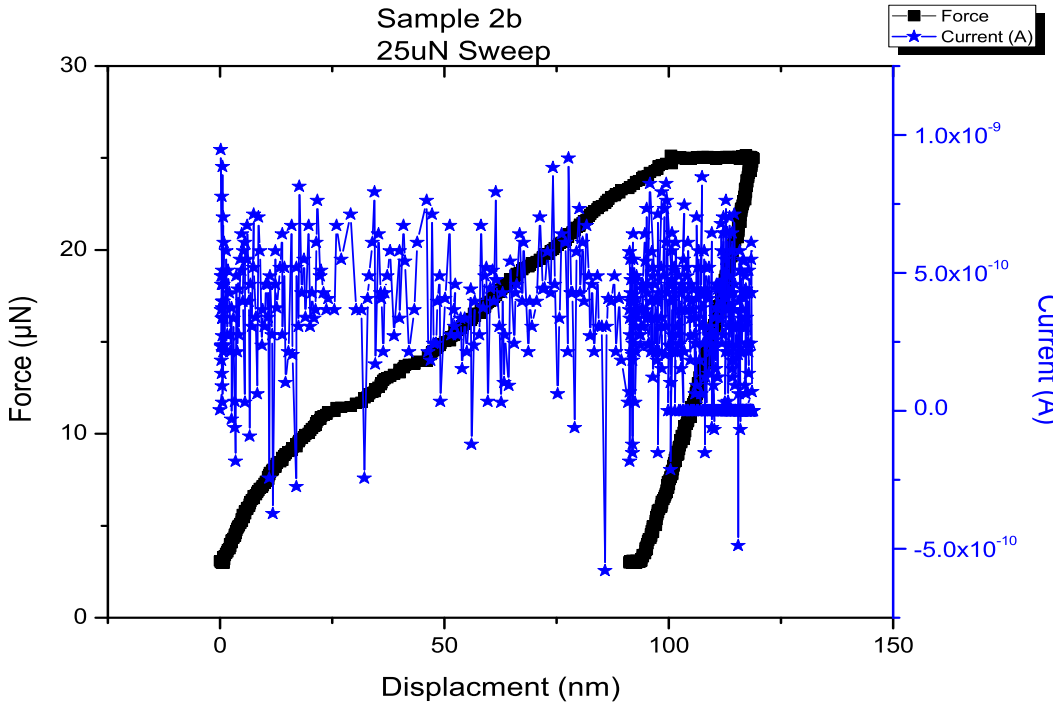

Figure 3.12: Graphical result - Sample 2b, 25uN

Data plot of PANI sample grown from HNO_3 *plus* 20 *wt% SWCNT with a max indenter load of* $25\mu N$.

we have $F = 25\ \mu N$ and $\delta = 95\ nm$, we conclude that
$a \simeq 378\ nm$,
and $p_{m,25_{2b}} \simeq 55.7\ MPa$.

Notice the depth of penetration is much greater in the SWCNT sample, along with the same reduction in conductance.

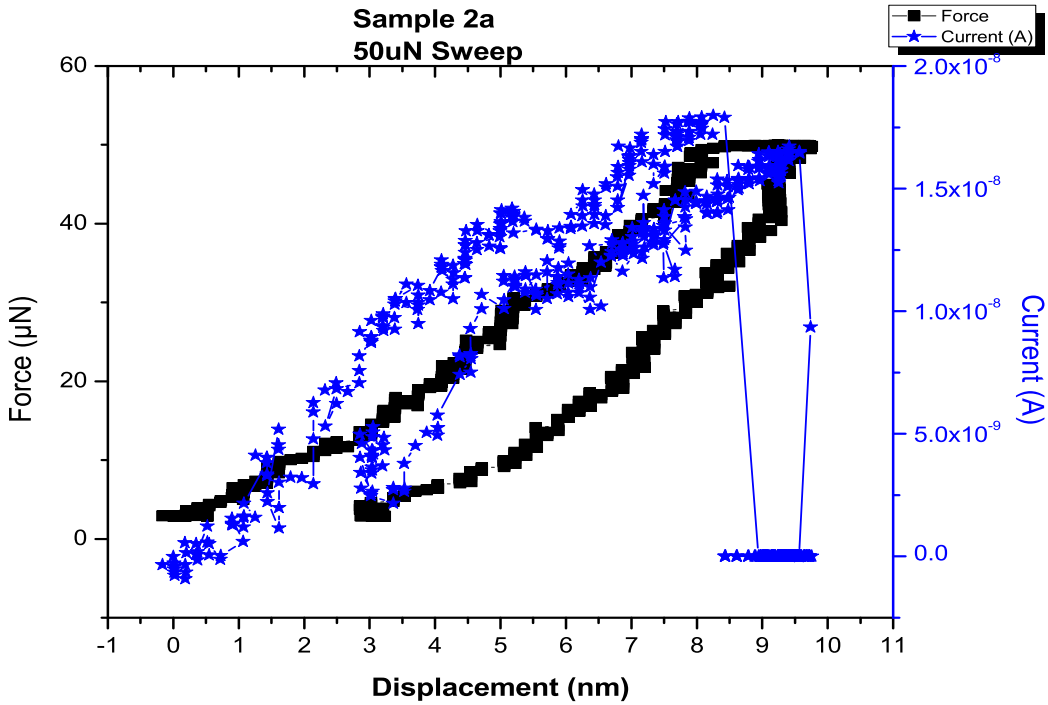

Figure 3.13: Graphical result - Sample 2a, 50uN

Data plot of PANI sample grown from HNO_3 with a max indenter load of $50\mu N$.

we have $F = 50\ \mu N$ and $\delta = 8.5\ nm$, we conclude that
$a \simeq 116\ nm$,
and $p_{m,50_{2a}} \simeq 1.18\ GPa$.

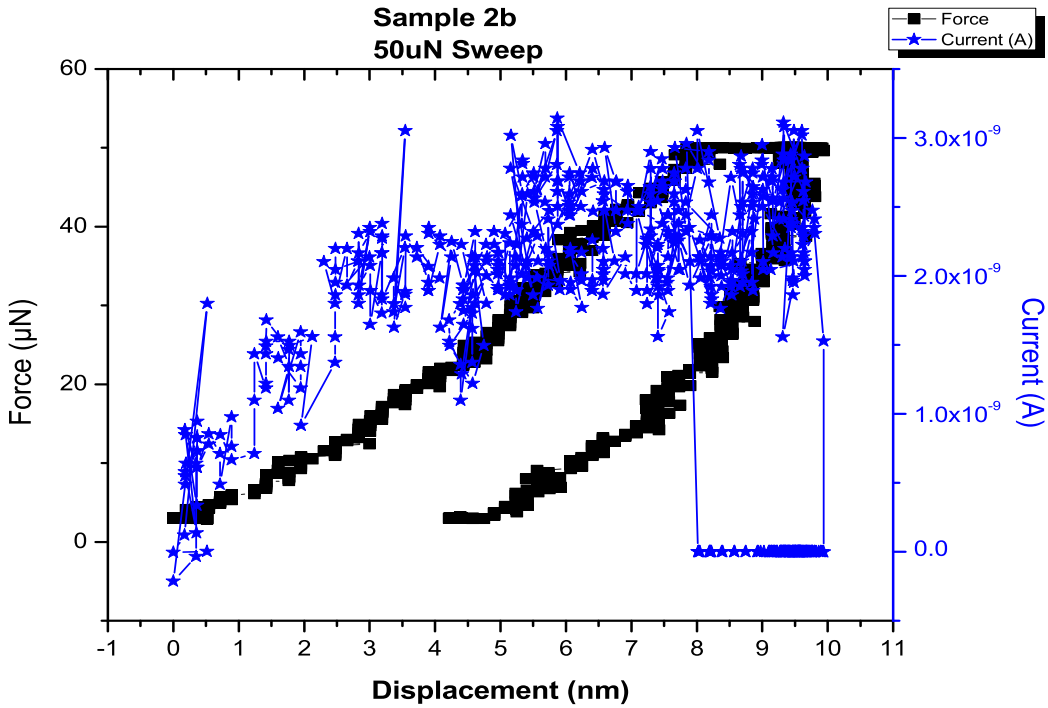

Figure 3.14: Graphical result - Sample 2b, 50uN

Data plot of PANI sample grown from HNO_3 plus 20 wt% SWCNT with a max indenter load of $50\mu N$.

we have $F = 50\ \mu N$ and $\delta = 8\ nm$, we conclude that
$a \simeq 113\ nm$,
and $p_{m,50_{2b}} \simeq 1.25\ GPa$.

Depth of penetration is nearly equivalent, yet the difference in conductance is much less in the SWCNT sample.

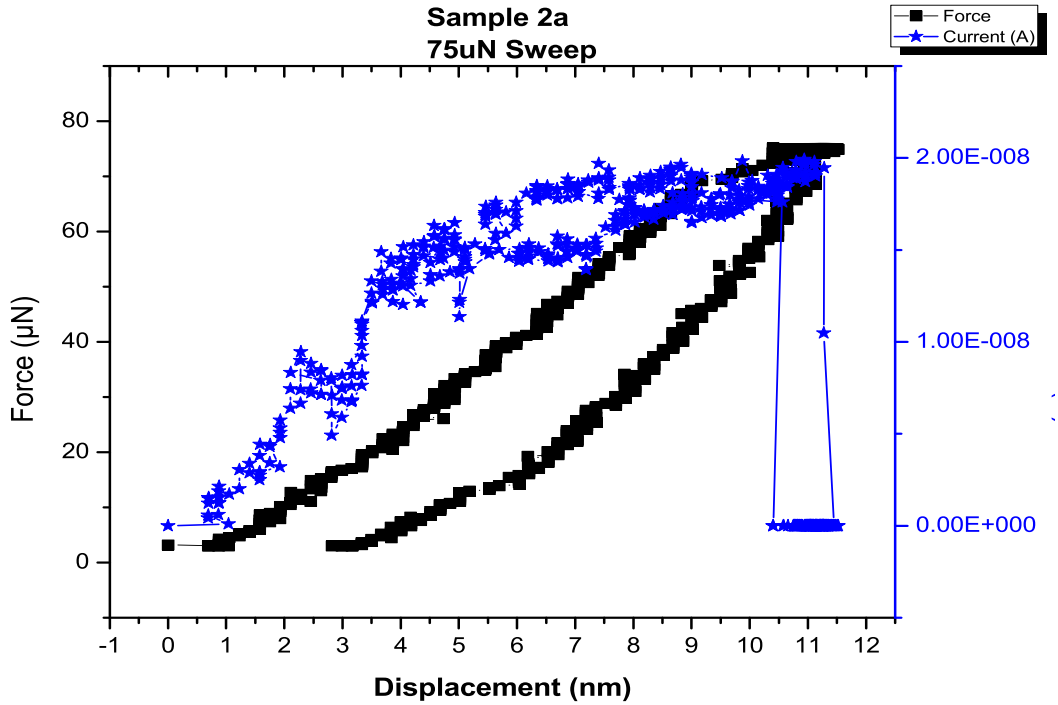

Figure 3.15: Graphical result - Sample 2a, 75uN

Data plot of PANI sample grown from HNO_3 with a max indenter load of $75\mu N$.

we have $F = 75\ \mu N$ and $\delta = 10.5\ nm$, we conclude that
$a \simeq 129\ nm$,
and $p_{m,75_{2a}} \simeq 1.43\ GPa$.

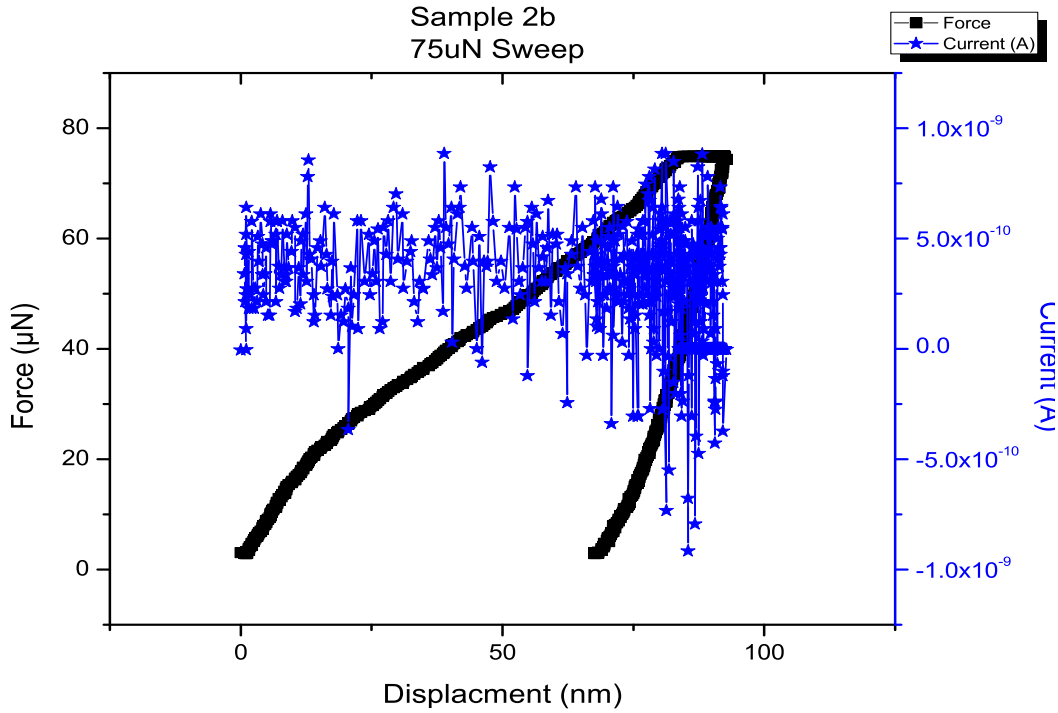

Figure 3.16: Graphical result - Sample 2b, 75uN

Data plot of PANI sample grown from HNO_3 plus 20 wt% SWCNT with a max indenter load of $75\mu N$.

we have $F = 75\ \mu N$ and $\delta = 80\ nm$, we conclude that
$a \simeq 349\ nm$,
and $p_{m,75_{2b}} \simeq 196\ MPa$.

The depth of penetration is much greater in the sample with SWCNT, yet the conductance is much less.

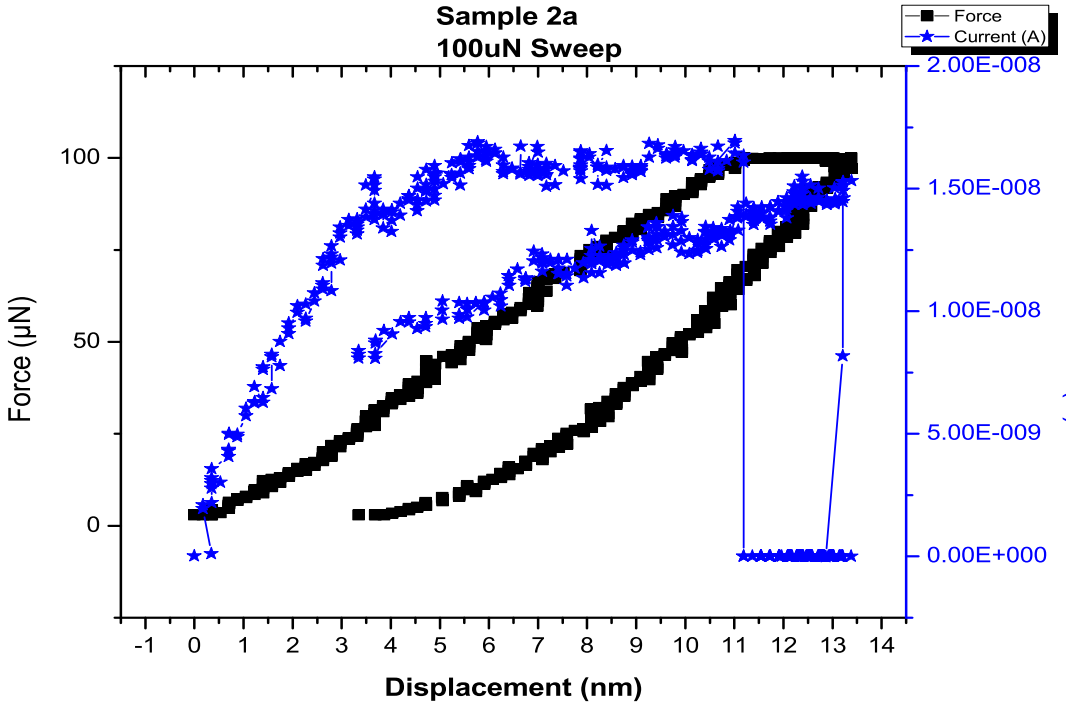

Figure 3.17: Graphical result - Sample 2a, 100uN

Data plot of PANI sample grown from HNO_3 *with a max indenter load of* $100\mu N$.

we have $F = 100\ \mu N$ and $\delta = 11\ nm$, we conclude that
$a \simeq 132\ nm$,
and $p_{m,100_{2a}} \simeq 1.82\ GPa$.

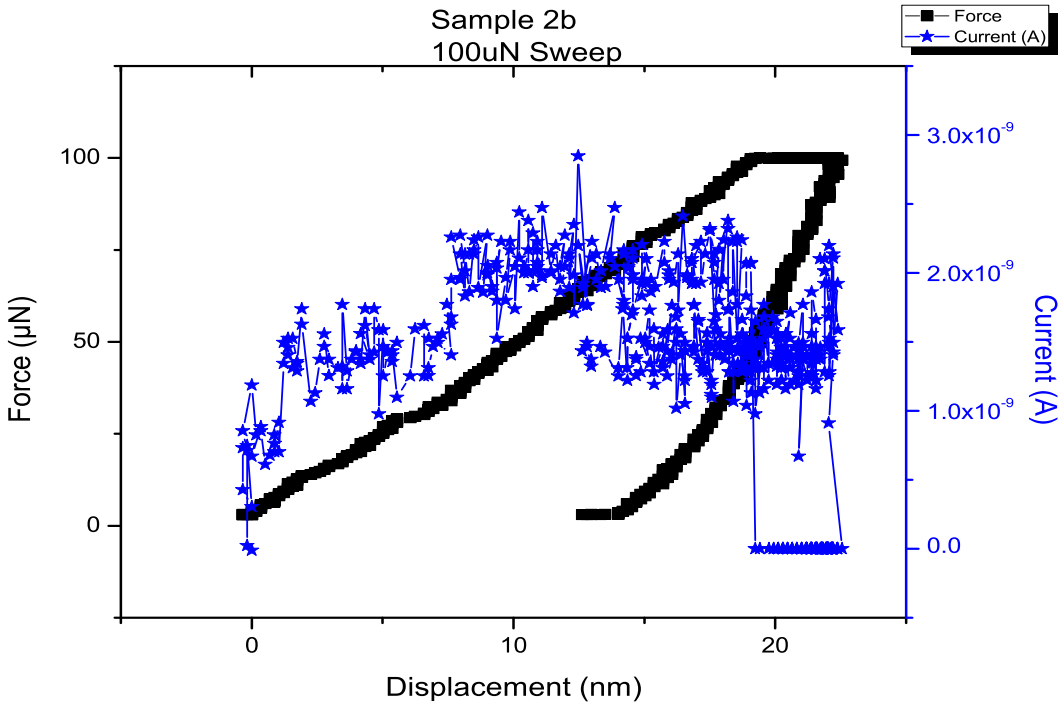

Figure 3.18: Graphical result - Sample 2b, 100uN

Data plot of PANI sample grown from HNO_3 *plus* 20 $wt\%$ *SWCNT with a max indenter load of* $100\mu N$.

we have $F = 100\ \mu N$ and $\delta = 19\ nm$, we conclude that
$a \simeq 173\ nm$,
and $p_{m,100_{2b}} \simeq 1.06\ GPa$.

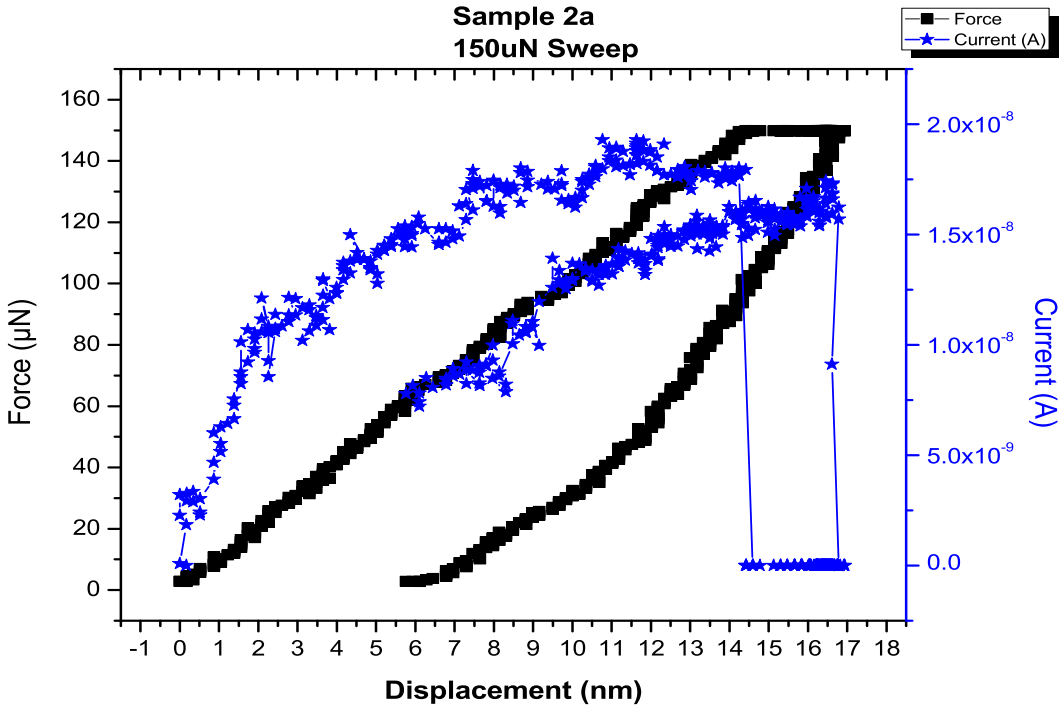

Figure 3.19: Graphical result - Sample 2a, 150uN

Data plot of PANI sample grown from HNO_3 *with a max indenter load of* $150\mu N$.

we have $F = 150\ \mu N$ and $\delta = 14\ nm$, we conclude that
$a \simeq 149\ nm$,
and $p_{m,150_{2a}} \simeq 2.15\ GPa$.

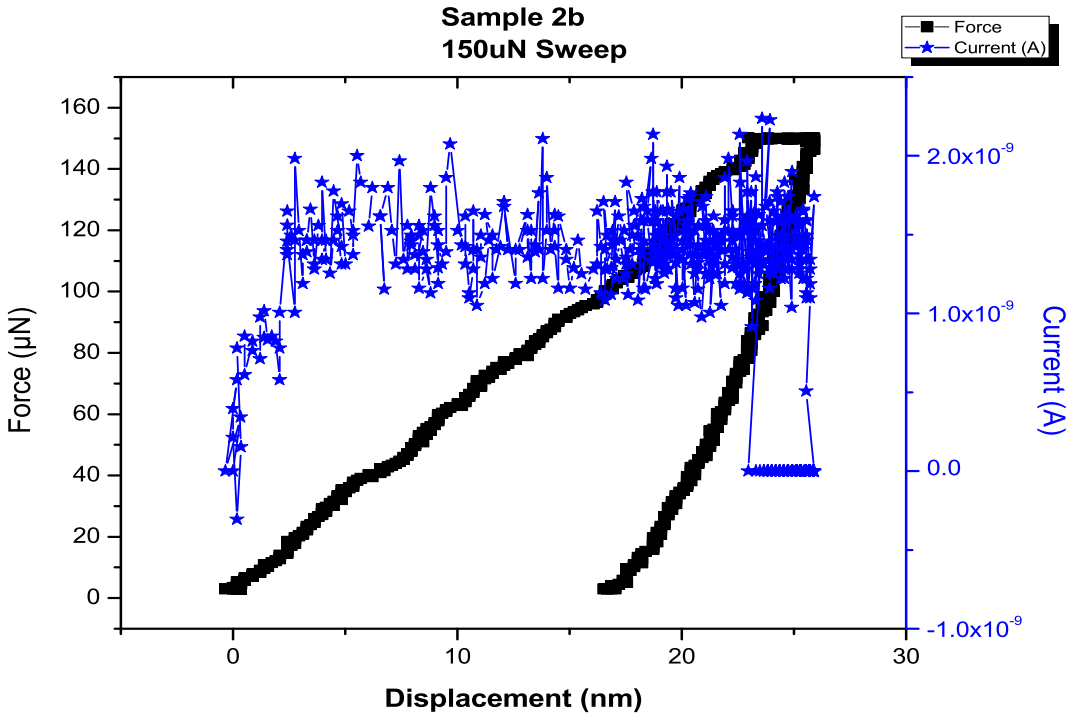

Figure 3.20: Graphical result - Sample 2b, 150uN

Data plot of PANI sample grown from HNO_3 plus 20 *wt% SWCNT with a max indenter load of* $150\mu N$.

we have $F = 150\ \mu N$ and $\delta = 23\ nm$, we conclude that
$a \simeq 190\ nm$,
and $p_{m,150_{2b}} \simeq 1.32\ GPa$.

3.3 Tabulated/Graphical Results

Tabulating the data, we have:

Table 3.1: Tabulated data - All results.

Sample ID - Load	a $[nm]$	p_m $[GPa]$	Current [A]		Sample ID - Load	a $[nm]$	p_m $[GPa]$	Current [A]
PANI (H_2SO_4)					PANI (H_2SO_4) + SWCNT			
1a - 25μN	78.9	1.28	7.0×10^{-7}		1b - 25μN	87.0	1.05	7.0×10^{-9}
1a - 50μN	138	0.835	7.5×10^{-7}		1b - 50μN	449	0.079	3.0×10^{-9}
1a - 75μN	144	1.16	8.1×10^{-7}		1b - 75μN	132	1.37	7.9×10^{-9}
1a - 100μN	144	1.54	8.0×10^{-7}		1b - 100μN	135	1.74	$-^*$
1a - 150μN	190	1.32	9.0×10^{-7}		1b - 150μN	178	1.51	9.0×10^{-9}
PANI (HNO_3)					PANI (HNO_3) + SWCNT			
2a - 25μN	93.6	0.907	1.9×10^{-8}		2b - 25μN	378	0.058	5.0×10^{-10}
2a - 50μN	116	1.18	1.8×10^{-8}		2b - 50μN	113	1.25	2.9×10^{-9}
2a - 75μN	129	1.43	2.0×10^{-8}		2b - 75μN	349	0.196	5.0×10^{-10}
2a - 100μN	132	1.82	1.7×10^{-8}		2b - 100μN	173	1.06	2.3×10^{-9}
2a - 150μN	149	2.15	1.9×10^{-8}		2b - 150μN	190	1.32	1.8×10^{-9}

$* =$ No reading due to equipment malfunction.

Tabulated data for all nanoindentation experiments conducted.

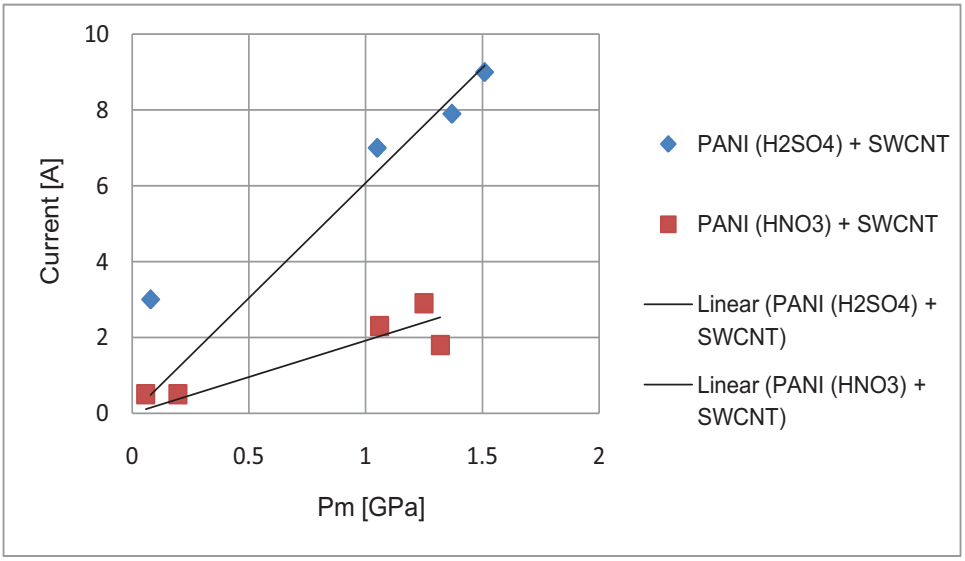

Figure 3.21: Graphical result - Electrolyte with SWCNT Comparison

Plot of the current versus the mean pressure. Notice the PANI (H_2SO_4)+SWCNT sample shows an increase in current three times that of the PANI (HNO_3)+SWCNT.

Chapter 4

Conclusion and Discussion

4.1 Contact Area

The tabulated results show a general trend of increased contact area between the indenter tip and the PANI sample as the load increases. This result is expected.

As the contact area increases the current tends to increase as well. The increase in current may also be attributed to a change in the morphology of the PANI film, as discussed by Adetunji et al. [21]. As pressure is applied, the PANI structure is transformed from a highly interconnected network into a continuous film. This transformation of the PANI film increases its conductivity due to the development of shorter conductance pathways with fewer resistive barriers.

4.2 Pressure Effects

Pressure effects are also evident from the data. Notice sample $1b - 50\mu N$; the mean pressure, p_m, is quite low. Subsequently, the current is also very low. This is due to the increased number of resistive barriers present in the highly interconnected film.

Conductivity of SWCNT is on the order of 40 $S\ cm^{-1}$, as reported by Karim and others [22]. Pure PANI has a conductivity of $\sim 0.35\ S\ cm^{-1}$. Thus the combination of the two should yield a conductivity in between. However, conductivity is a strong function of the microstructure of the resultant PANI and SWCNT film. A stable suspension of the SWCNT in the PANI polymer matrix is critical for a conducting film [22].

Unstable suspension may lead to voids and discontinuities within the SWCNT-PANI structure.

This relationship of conductivity versus microstructure can be seen in Figure 3.22 where the conductivity is compared to the mean pressure of the contact. This figure is a direct result of the data from Table 3.21. As the mean pressure of the contact increases, the conductivity increases linearly with the slope where the material processed with the H_2SO_4 electrolyte being about a factor of three greater than that using the HNO_3 electrolyte. This strongly suggests that the initial void or fault contact in the HNO_3 processed film was initially much greater.

In this study, the current for the SWCNT films is on the order of two magnitudes less than the neat films. This could be the result of voids and discontinuities within the microstructure of the film. The level of intimacy between the PANI polymer and the SWCNT is a direct result of the processing steps taken when combining them together. Improper processing will lead to air gaps in the microstructure, resulting in a decrease in current flow.

Voids in the microstructure may also be the reason why three trials, specifically $1b - 50\mu N$, $2b - 25\mu N$, and $2b - 75\mu N$, show a very high contact area. The voids allow deeper penetration of the tip into the polymer.

4.3 Recommended Future Work

Future work should be carried out to characterize the microstructure. The SWCNT-PANI structure can be quite complex and can be properly characterized through the use of elemental analysis (EA), X-ray photoelectron spectroscopy (XPS), Fourier transform infrared (FT-IR), field emission scanning electron microscopy (FE-SEM), thermal gravimetric analysis (TGA), electron spin resonance (ESR), X-ray diffraction (XRD) and transmission electron microscopy (TEM).

SEM imaging will pictorially reveal the uniformity of the SWCNT-PANI matrix. One could compare the images from SEM to others in literature ensuring that the PANI film morphology appears globular and mostly continuous. The SEM images of the SWCNT-PANI samples should reveal PANI chains connected with SWCNT rods.

Employing EA would allow one to verify the existence and dominance of certain

elements. Carbon content is dominated by the SWCNT and the nitrogen content is contributed by the PANI.

TEM would allow for the observation of any interaction effects between the SWCNT and the PANI polymer. Interaction of these two will change the conductivity results of the composite.

FT-IR would confirm the existence of the covalent bonds present in the PANI film, the SWCNT, and the SWCNT-PANI composite. Any interactions that form chemical bonds between the SWCNT and PANI would then be visible and help explain any increase or decrease in conductivity.

Polaron and bipolaron as charge carriers can be distinguished through the use of ESR [22]. The presence of polarons in PANI can be observed. The SWCNT-PANI composite ESR data is typically dominated by the PANI. This is due to the SWCNT having almost no ESR data (nearly silent).

XRD would help characterize the microstructure of the PANI and reveal how much crystallinity is in the polymer itself. Observing the XRD of the composite shows any interaction effects and can give information as to what material is dominating the microstructure.

Thermal stability of the materials is observed via TGA. Measuring both the PANI and SWCNT would show a thermal reference to their individual responses. Comparing these to the composite would show how uniform the microstructure is.

XPS can also be used to determine any interaction effects from the SWCNT in the PANI film.

References

[1] A. Brent Strong. *Plastics: Materials and Processing.* Prentice-Hall, Inc., New Jersey, 2000.

[2] W. D. Callister. *Material Science and Engineering: An Introduction.* Wiley, John & Sons, Incorporated, New Jersey, 2006.

[3] J. A. Brydson. *Plastics Materials.* Butterworths, London, 1989.

[4] Prasanna Chandrasekhar. *Conducting polymers, fundamentals and applications: a practical approach.* Kluwer Academic Publishers, Massachusetts, 1999.

[5] Alan G. MacDiarmid. Synthetic metals: a novel role for organic polymers. *Synth. Met.*, 125:11–22, 2002.

[6] Liu C.X. Pinto N.J. Bao, Z.-X. P(ani)? *Synth. Met.*, 87:147, 1997.

[7] E. Alfredo Campo. *The complete part design handbook: for injection molding of thermoplastics.* Hanser, Munich, 2006.

[8] J. R. Davis. *Metals handbook.* ASM International, Ohio, 1998.

[9] Howard E. Boyer. *Hardness Testing.* ASM International, Ohio, 1987.

[10] Jozsef Karger-Kocsis and Stoyko Fakirov. *Nano- and Micro- Mechanics of Polymer Blends and Composites.* Hanser, Munich, 2009.

[11] G.M. Swallowe. *Mechanical Properties and Testing of Polymers.* Kluwer Academic Publishers, Netherlands, 1999.

[12] Anthony C. Fischer-Cripps. *Nanoindentation.* Springer, New York, 2004.

[13] John T. DeWolf Ferdinand P. Beer, E. Russell Johnston Jr. *Mechanics of Materials*. McGraw-Hill, New York, 1992.

[14] Johann Desilvestro and Werner Scheifele. Morphology of electrochemically prepared polyaniline. *J. Mater. Chem.*, 3:263–272, 1993.

[15] Alan G. MacDiarmid Wu-Song Huang, Brian D. Humphrey. Polyaniline, a novel conducting polymer. *J. Chem. Soc., Faraday Trans. 1*, 82:2385–2400, 1986.

[16] Cunha A M Viana J C and Billon N. The effect of skin thickness and spherulite on the mechanical properties of injection moldings. *J Mater Sci*, 36:4411–4418, 2001.

[17] Gorbunov A A and Skvortsov A M. Statistical properties of confined molecules. *Adv Coll Interf Sci*, 62:31–108, 1995.

[18] M. A. Mohamoud. Conducting polymers: Smart materials with nanotechnology applications. *SPE Plastics Engineering*, 64:32–38, 2008.

[19] Hysitron, Inc., 10025 Valley View Rd., Minneapolis, MN, 55344.

[20] Douglas D. Stauffer and William W. Gerberich. Ph.d. dossier. 2008.

[21] N.-R. Chiou O.O. Adetunji and A.J. Epstein. Effect of pressure on the morphology of polyaniline nanostructures. *Synthetic Metals*, 159:2263–2265, 2009.

[22] Young-Tae Park Mu S. Lee Mohammad R. Karim, Chul J. Lee. Swnts coated by conducting polyaniline: Sythesis and modified properties. *Synth. Met.*, 151:131–135, 2005.